

APPLICATION OF ATTOSECOND TECHNIQUES TO CONDENSED MATTER SYSTEMS

DISSERTATION

Presented in Partial Fulfillment of the Requirements for the Degree Doctor of
Philosophy in the Graduate School of The Ohio State University

By

Gregory J. Smith, M.Sc.

Graduate Program in Physics

The Ohio State University

2019

Dissertation Committee:

Louis F. DiMauro, Advisor

L. Robert Baker

Jay A. Gupta

Yuri V. Kovchegov

© Copyright by

Gregory J. Smith

2019

Table of Contents

	Page
List of Figures	iii
1 Condensed Matter XUV Transient Absorption Experiments	1
1.1 Statement of Contribution	1
1.2 Introduction	1
1.3 Relative Contributions of Real and Imaginary Parts of \tilde{n}	5
1.4 Sample Requirements and Geometry	9
1.5 Absorbance and Transient Absorbance Data Collection Methods	10
1.6 The Supporting Nitride Membrane	15
1.7 The Germanium Sample	19
1.8 IR Pump Arm Considerations	21
1.8.1 Calculation of IR Intensity at Focus	21
1.8.2 Estimation of Excited Carrier Density	23
1.8.3 The XUV-IR Overlap Integral	25
1.9 Experimental Methods	28
1.9.1 Finding XUV-IR spatial overlap	28
1.9.2 Finding XUV-IR Temporal Overlap	33
1.9.3 Optimization of IR Pump Parameters	33
1.10 Data Processing	48
1.10.1 energy and delay calibration	49
1.10.2 A note about the Jacobian	49
1.10.3 source of noise	50
1.10.4 sample drilling or random drift?	50
1.10.5 correlations between harmonic peaks in ΔA	50
1.10.6 integration vs summation near harmonic peaks	50
1.10.7 apparent ω and 2ω oscillations in data	50
Chapters	
Bibliography	51

List of Figures

Figure	Page
1.1 Schematic of the Transient Absorption BeamLine (TABLE). Blue shaded region represents vacuum. BS: beam splitter, S: computer-controlled shutter, L: lens, I: iris, 2ω : optics for 2ω generation, HHG: high harmonic generation, F: metallic filter, EM: ellipsoidal mirror, HM: hole mirror, SH: sample holder, CF: long-pass color filter, WP: $\lambda/2$ waveplate, P: wire-grid polarizer, W: delay wedges, PD: photodiode and associated optics, DG: dispersive grating, MCP/P: micro-channel plate and phosphor.	2
1.2 Schematic of an attosecond transient absorption spectroscopy (ATAS) experiment. An IR laser pulse excites electrons in the material, driving them across the band-gap. An XUV pulse passes through the sample after a delay Δt . The measured XUV absorbance is sensitive to electronic populations and states. Figure taken from [13].	3
1.3 Normal and non-normal incident geometries. a) Normal incidence geometry showing Fresnel coefficients R_F , T_F for interfaces and total transmission T and reflectance R for a slab of thickness h . Figure recreated from [11]. b) Non-normal geometry showing definitions of angles θ_i , θ_r and θ_t with respect to each interface.	5
1.4 Consequences of ignoring the real part of \tilde{n} when calculating the transmission T of a thin sample. Top panel: complex refractive index of silicon using the notation from Eq. (1.1). The Si L -edge absorption feature is visible near 100 eV. Data from [6]. Bottom panel: relative error in T , as defined in Eq. (1.8), introduced by ignoring the contribution of $\text{Re}(\tilde{n})$. An infinite number of bounces (e.g., Eq. (1.6)) is assumed.	6
1.5 Calculated XUV transmission of various materials. Data from [6].	9
1.6 Calculated XUV transmission of various metallic filters. Data from [6].	11
1.7 Schematic of competing raster methods, shown in the sample's reference frame. The clear aperture of the sample is represented by the interior of the black square. The laser propagation direction is out of the page. The laser focal spots are shown as red circles, and the movement of the sample holder relative to the laser focus is indicated by arrows. This diagram is to scale for a $1 \times 1 \text{ mm}^2$ clear aperture sample, a $60 \mu\text{m}$ diameter IR focal spot and a $200 \mu\text{m}$ step size.	11

1.8	XUV transmission measurements of Al metallic filter and silicon nitride membrane. Left panel: normalized XUV counts for i) unfiltered HHG signal, ii) HHG going through a 200 nm Al filter and iii) HHG going through a 200 nm Al filter and 30 nm of silicon nitride. Counts are scaled by the Jacobian (Eq. (1.27)). Right panel: transmission curves obtained from the left panel's data. Also shown are literature values for 20 nm of silicon nitride and 200 nm of Al with two 4 nm oxide layers [6]. Multilayer interference is not taken into account. Oscillations in measured transmission are numerical artifacts which will be discussed in the text.	15
1.9	XUV transmission map of 30 nm silicone nitride freestanding membrane. Left panel: integrated harmonic peaks in the range ?? – ?? eV. Sample holder motor positions are indicated by x- and y-positions. Right panel: histogram of logarithmic deviation of counts from the average. Dashed line shows a normal distribution.	16
1.10	Cartoon showing the cross section of the free standing sample heterostructure. A 500 μm thick Si frame supports a freestanding 30 nm low stress silicon nitride membrane (Norcada QX7300X), upon which 100 nm of germanium has been deposited. The Si frame has a 3x3 mm^2 square clear aperture and a 7.5x7.5 mm^2 square external dimension. The taper of the Si frame thickness along the perimeter of the clear aperture forms a knife edge. In an ATAS experiment, the XUV and IR pulses propagate from the top to bottom of the figure.	16
1.11	Band structure and orbital character of germanium. Purple arrows indicate XUV-induced transitions from the 3d core levels to the valence bands. Red arrow indicates IR-induced transition across the direct band gap. Figure adapted from [16].	19
1.12	Measured ground absorbance A of a 100 nm Ge film on a 30 nm silicon nitride membrane. The contribution of the membrane has been subtracted. Blue line is the measured absorbance A . The red dashed line shows the result of numerical filtering to eliminate numerical artifacts (described in main text).	20
1.13	Numerical propagation of the IR ($\lambda=1500 \text{ nm}$) beam through the pump arm. Beam path layout follows Fig. 1.1. Each panel shows the intensity of the beam as the beam propagates towards the focus. The first panel shows the measured intensity (Electrophysics PV320 thermal camera), all other panels are calculations. The arrows on the lineout indicate FWHM. All calculations are for vacuum ($n=1$). See text for details.	22
1.14	XUV-IR overlap function, as defined in Eq. (1.19), calculated using the numerical simulation results of Fig. 1.13 and a Gaussian XUV beam with a 6 μm waist. The result has been normalized to perfect overlap. NOTE: change the y-axis label to something like a/a_{max}, and the x-axis label to x_0.	23
1.15	Schematic of XUV knife edge measurement. EM: ellipsoidal mirror, z_0 : XUV focal plane.	29
1.16	A typical XUV knife edge measurement near the focal plane. The sample motor position is $k = 11.0000 \text{ mm}$. A fit to equation Eq. (1.23) yields a beam waist of 10.82 μm at this position.	29

1.17 Evolution of XUV beam waist as a function of propagation direction, z . The Rayleigh range z_R and beam waist w_0 are extracted from the fit to Eq. (1.22). question: what is M^2 value of the XUV?	30
1.18 <i>In-situ</i> imaging of the samples within the target chamber. Left: optical setup for <i>in-situ</i> imaging of samples. C: Si CCD camera, HM: hole mirror, SH: sample holder, FM: flip mirror, L: lens. Right: false color image showing the sample holder with a 3 x 3 grid of 5 mm diameter clear apertures. Samples are held in a clamshell design centered in the clear apertures. Samples are backlit using a flashlight.	34
1.19 False color images showing laser drilled freestanding membranes. Left: pristine 260 nm thick Si membrane (Norcada). Middle: same sample, after performing an IR power scan that exceeded the membrane's damage threshold. A $<200 \mu\text{m}$ hole is visible as a cluster of bright pixels near the center of the membrane. Right: 30 nm SiN membrane after a similar power scan showing a "popped" membrane. The ragged edges near the clear aperture of the frame are all that remain of the membrane. For all images, the apparent brightness gradient across the samples is caused by inconsistent backlighting. Images were taken using the optical setup shown in the left panel of Fig. 1.18.	34
1.20 Laser damaged 200 nm silicon membrane samples. Left panel: XUV map of pristine Si before being exposed to IR laser. Higher transmission is indicated by brighter colors. Sample is rotated approximately 30 degrees relative to motor axes. Center panel: XUV map of damaged sample after being pumped with $\approx 65 \mu\text{J}$ of $\lambda = 1500 \text{ nm}$ at 1 kHz rep. rate in two locations. Damage occurred within the first camera exposure (2 seconds) and propagated to regions that were not exposed to the laser. Right panel: microscope image of damaged sample (beige) showing large sections of missing material (white). Red circles in all three pictures indicate the two locations that were exposed to IR laser light.	35
1.21 1 kHz fixed-delay ATAS measurements on 100 nm Ge using a $\lambda = 1450 \text{ nm}$ excitation pulse. See text for details.	37
(a) $\tau \approx 0 \text{ fs}$, PE = 1.03 μJ .	37
(b) $\tau \approx 0 \text{ fs}$, PE = 1.43 μJ .	37
(c) $\tau = -\infty$, PE = 1.03 μJ .	37
(d) $\tau = -\infty$, PE = 1.43 μJ .	37
(e) PE = 1.03 μJ .	37
(f) PE = 1.43 μJ .	37

1.22	1 kHz ATAS measurements in Ge using a $\lambda = 1450$ nm excitation pulse. Fig. 1.22a: fixed-delay ATAS measurements with a pulse energy of 1.75 μJ . Fig. 1.22b: Pulse energy scaling at overlap of 1 kHz measurements. Figs. 1.22c to 1.22f: delay scans at 1 kHz. Figs. 1.22c and 1.22d: raw delay scan data. Figs. 1.22e and 1.22f: rolling average of the raw data with a 65 fs window (20 delay points). The left panel on each spectrogram shows the XUV spectrum. See text for details.	38
(a)	$\tau \approx 0$ fs, PE = 1.75 μJ .	38
(b)	PE scaling at $\tau \approx 0$ fs.	38
(c)	PE = 1.43 μJ .	38
(d)	PE = 1.75 μJ .	38
(e)	PE = 1.43 μJ (rolling average).	38
(f)	PE = 1.75 μJ (rolling average).	38
1.23	500 kHz ATAS measurements in Ge using a $\lambda = 1450$ nm, 1.67 μJ excitation pulse. Each delay curve is an average of 104 identical measurements. The sample shows no delay dependance within the uncertainty of the measurement.	39
1.24	125 Hz ATAS measurements in Ge using a $\lambda = 1450$ nm, 2.64 μJ excitation pulse. Each lineout represents the average of 394 measurements. See text for details.	39
1.25	125 Hz delay scan in Ge using a $\lambda = 1450$ nm, 2.74 ± 0.35 μJ excitation pulse. This is an average of 3 repeated measurements. See text for details.	40
1.26	125 vs. 250 Hz measurements at $\lambda = 1430$ nm.	40
(a)	125 Hz ($M = 6$)	40
(b)	250 Hz ($M = 2$)	40
1.27	Pulse energy scan of 100 nm germanium sample near temporal overlap. Left panel shows the average ground state spectrum, $S_{gs}(E)$. Right panel shows the change in absorbance, $\Delta A(E, PE)$, as a function of pulse energy, PE. Data shown in this figure is the average of 20 identical measurements: individual datasets were background subtracted and normalized for exposure time before being averaged; no additional data processing was performed on this dataset. See text for details.	41
1.28	Left panel: spatial mapping of integrated XUV counts (integrated over what energy range?) of a 100 nm Ge + 30 nm silicon nitride sample. Right panel: histogram of values from the left panel.	44
1.29	this figure shows the data processing pipeline. it shows how we start with PumpOn-Off 2D images and transform them into spectrograms. it includes steps like an absorbance (A) calculation, spectral lineouts, frequency filtering and smooth, energy calibration, etc.	44
1.30	this figure shows, using real data, a pump off and pump on spectral lineout. in another panel, it shows the ΔA .	45
1.31	$N = 50$ averaged delay scans. no corrections have been made to the data	45
1.32	$N = 50$ averaged delay scans. no corrections have been made to the data. histogram of ΔA for 3 selected features. dataset is same as Fig. 1.31.	45
1.33	correction factor, $C(\tau, E)$, from Eq. (1.28).	46
1.34	histogram of correction factor, $C(\tau, E)$, values from Eq. (1.28).	46

1.35 histogram of spectral features from dataset with correction factor $C(\tau, E)$ applied	47
1.36 normalized dataset: dataset with correction factor $C(\tau, E)$ applied	47
1.37 normalized dataset with frequency filter applied	47

Chapter 1

CONDENSED MATTER XUV TRANSIENT ABSORPTION EXPERIMENTS

1.1 Statement of Contribution

This experiment uses home-made equipment consisting of a XUV-IR Mach-Zhender interferometer, a bright XUV light source, a target chamber and an XUV photon spectrometer. The entire apparatus was designed and built by Gregory Smith and Stephen Hageman. Dietrich Kiesewetter helped test and improve the stability of the interferometer. The LabView software controlling the spectrometer's detector and shutters was programmed by Kent Talbert. The vacuum system's safety system was designed and programmed by Andrew Piper. The germanium samples were grown by Dr. Yaguo Tang. Transient absorption experiments were done by Gregory Smith and Stephen Hageman. Analysis presented in this document was done by Gregory Smith. Further details on the apparatus and the relevant physics will be discussed in the main dissertation.

1.2 Introduction

We generate extreme ultraviolet (XUV) light using an extremely non-linear process called *high harmonic generation* (HHG). Briefly, the XUV light source can be thought of as a frequency comb spanning from ~ 20 eV to $\sim 50 - 150$ eV. Depending on the generation conditions, the separation between the teeth of the frequency comb is either ω or 2ω , where

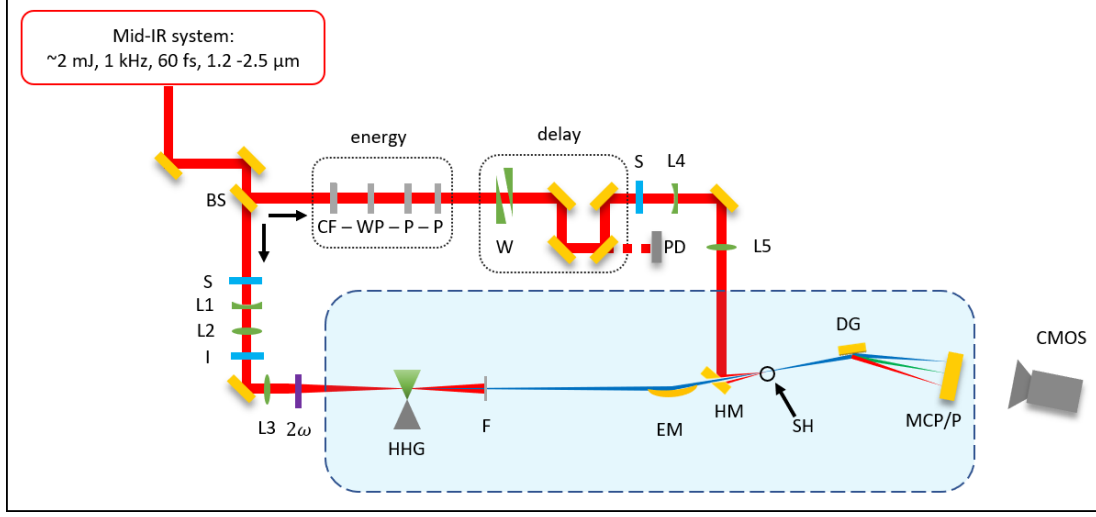


Figure 1.1: Schematic of the Transient Absorption BeamLine (TABLE). Blue shaded region represents vacuum. BS: beam splitter, S: computer-controlled shutter, L: lens, I: iris, 2ω : optics for 2ω generation, HHG: high harmonic generation, F: metallic filter, EM: ellipsoidal mirror, HM: hole mirror, SH: sample holder, CF: long-pass color filter, WP: $\lambda/2$ waveplate, P: wire-grid polarizer, W: delay wedges, PD: photodiode and associated optics, DG: dispersive grating, MCP/P: micro-channel plate and phosphor.

ω is the frequency of our laser light. In the time domain, the XUV is a train of attosecond bursts of broadband light with an envelope of ~ 50 fs. This XUV light is phase locked to the field that generated it, so it this process can be used within an interferometer with sub-cycle stability. Due to the ionizing nature of XUV light, the entire experiment must be performed under vacuum.

The experiment is powered by a commercial mid-IR laser system (Spectra Physics Spitfire ACE, which delivers 12 mJ of 800 nm light at 100 – 1,000 Hz repetition rate, ~ 65 fs duration. This light is sent into a commercial optical parametric amplifier (Light Conversion HE TOPAS Prime), which converts it to longer wavelengths ($1.2 - 2.5 \mu\text{m}$, ≈ 2 mJ) while roughly maintaining pulse duration. The output of the TOPAS is routed into a Mach-Zhender interferometer, shown in Fig. 1.1. A beam splitter (BS) delivers the bulk of the pulse energy (96%) to the generation arm of the interferometer, which contains the HHG source and specialized XUV focusing optics. A small percentage of TOPAS's pulse energy goes to the pump arm, which contains optics to control the pulse energy, relative

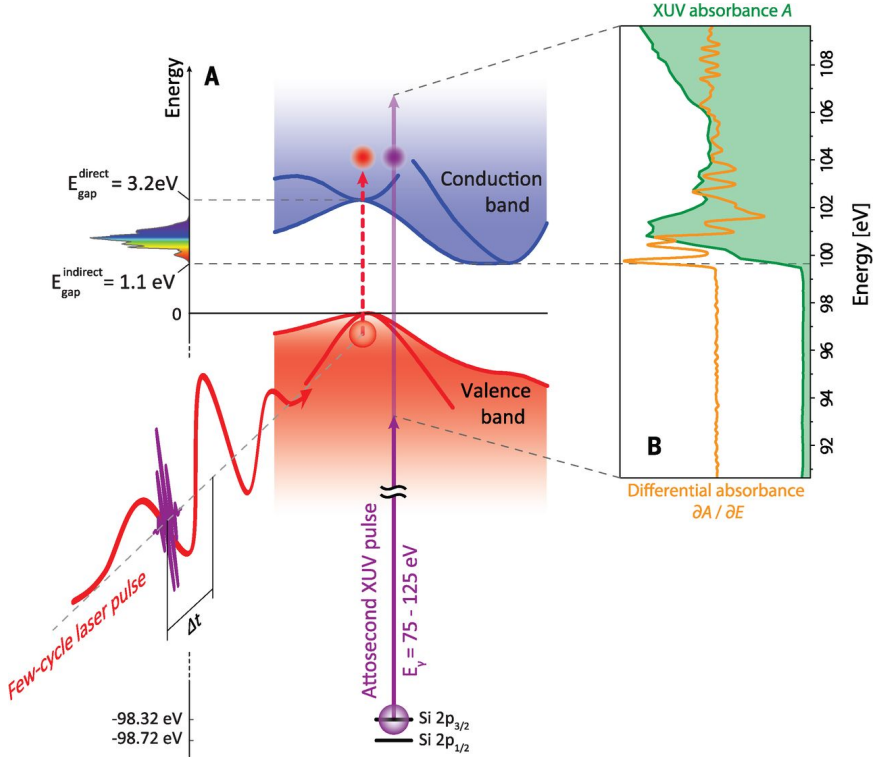


Figure 1.2: Schematic of an attosecond transient absorption spectroscopy (ATAS) experiment. An IR laser pulse excites electrons in the material, driving them across the band-gap. An XUV pulse passes through the sample after a delay Δt . The measured XUV absorbance is sensitive to electronic populations and states. Figure taken from [13].

delay between the two arms, and focusing optics. The pump arm is routed into the vacuum system, where a silvered hole mirror (HM) combines the two arms of the interferometer in a collinear fashion. This optic is designed to allow the XUV light to pass through a clear aperture on the backside of the HM while the pump arm's IR light reflects off the front face. The interferometer is aligned so that both arms have a common focus in the target chamber at the sample holder (SH).

The basic concept of an *attosecond transient absorption spectroscopy* (ATAS) experiment is shown in Fig. 1.2. In this experiment, a sample is placed at the combined XUV/IR focus in a transmission (normal) geometry. An XUV photon spectrometer is placed behind the sample and the transmitted XUV spectrum S is measured as a function of XUV-IR delay. The IR light is not measured by the spectrometer.

Fundamentally, changes in photoabsorption correspond to electron and phonon dynamics. In a condensed matter material, these processes occur on the picosecond (10^{-12} s), femtosecond (10^{-15} s) and even attosecond (10^{-18} s) time scales [4, 13, 15, 16]. At XUV energies, photons drive electronic transitions from a core-level state to one near the Fermi level, which requires electron population in the initial state and a vacancy in the final state. Because the initial state is tens or even hundreds of eV below the bandgap, it is shielded from the external IR field. The final states, being closer to the Fermi level, enjoy no such shielding. Therefore they can be distorted by the external IR field, and the electron population can be transferred across the bandgap in response to it. After an initial IR excitation, electrons relax via different scattering channels, including with other electrons or phonon modes with longer lifetimes. Provided the selection rules allow it, the photoabsorption spectrum is sensitive to all of these dynamics. Thus by measuring the XUV spectrum as a function of XUV-IR delay, we can track the electronic and phononic response of a sample to an ultrafast IR excitation.

This chapter will discuss with the experimental considerations and methods associated with an ATAS experiment.

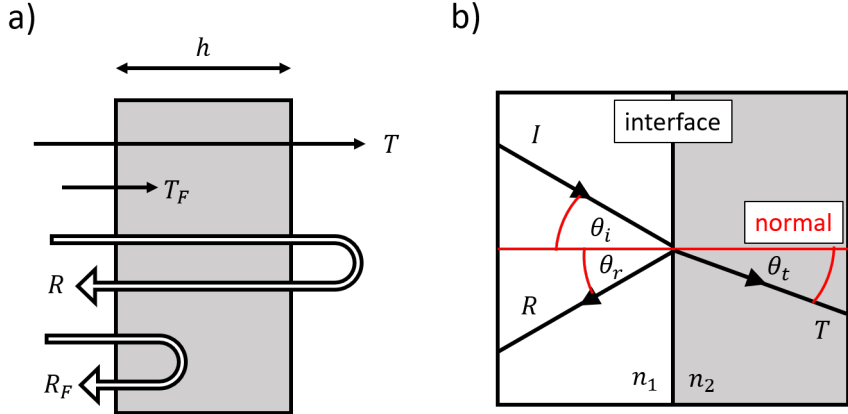


Figure 1.3: Normal and non-normal incident geometries. **a)** Normal incidence geometry showing Fresnel coefficients R_F , T_F for interfaces and total transmission T and reflectance R for a slab of thickness h . Figure recreated from [11]. **b)** Non-normal geometry showing definitions of angles θ_i , θ_r and θ_t with respect to each interface.

1.3 Relative Contributions of Real and Imaginary Parts of \tilde{n}

In a transient absorption experiment, we measure the transmission T . Generally speaking, T depends on both parts of the complex refractive index: $\tilde{n} = n + ik$. However, in a normal transmission geometry it turns out that the contribution of $\text{Im}(\tilde{n})$ dominates the measured signal, and to a good approximation the role of $\text{Re}(\tilde{n})$ can be ignored. Note that in a non-normal reflection geometry, both parts of \tilde{n} make significant contributions to the measured signal. In the following discussion we will analyze the Fresnel equations to see why this is the case. This section will draw from arguments made in reference [11].

First, we consider the normal geometry shown in the left panel of Fig. 1.3. We write the complex index of refraction in the following form:

$$\begin{aligned}\tilde{n} &= n - ik \\ &= (1 - \delta) - i\beta\end{aligned}\tag{1.1}$$

The Fresnel coefficients R_F and T_F describe the interface reflectance and transmittance and

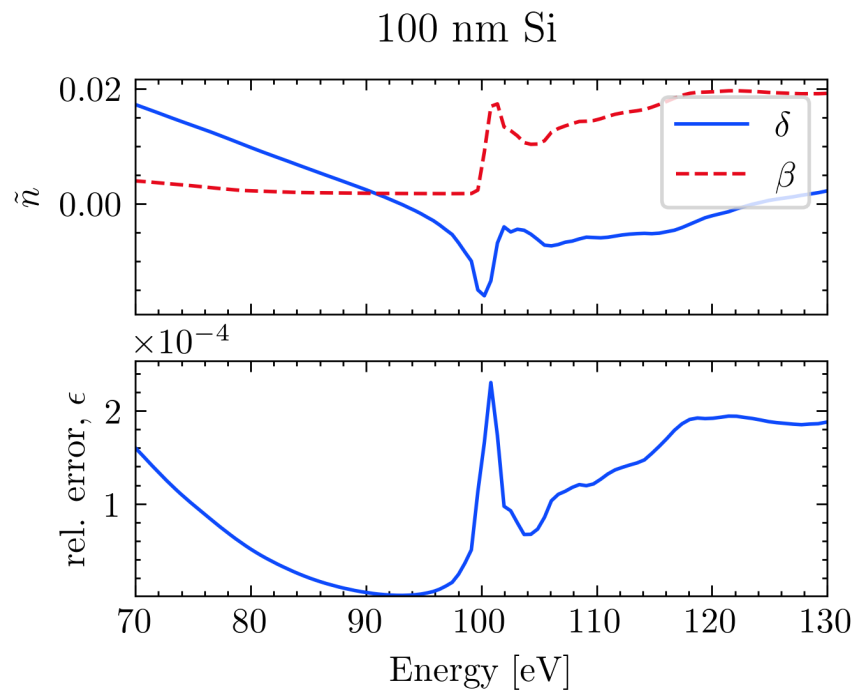


Figure 1.4: Consequences of ignoring the real part of \tilde{n} when calculating the transmission T of a thin sample. Top panel: complex refractive index of silicon using the notation from Eq. (1.1). The Si L -edge absorption feature is visible near 100 eV. Data from [6]. Bottom panel: relative error in T , as defined in Eq. (1.8), introduced by ignoring the contribution of $\text{Re}(\tilde{n})$. An infinite number of bounces (e.g., Eq. (1.6)) is assumed.

depend on both parts of the complex index \tilde{n} . For normal incidence, they are:

$$R_F = \left| \frac{n - ik - 1}{n - ik + 1} \right|^2 \quad (1.2)$$

$$T_F = \frac{4n}{|n - ik + 1|^2}$$

Absorption in the bulk is described via the absorption length α :

$$\alpha = 4\pi k / \lambda \quad (1.3)$$

Ignoring interface effects, the transmisison through the bulk is:

$$T_{\text{bulk}} = \exp(-\alpha h) \quad (1.4)$$

Note that α and T_{bulk} only depend on k .

The total reflectance R and transmission T are the result of interface effects plus bulk effects. We must consider the case where the detected light is the result of multiple reflections within the sample. Neglecting interference, we consider the case of $2N$ bounces where the laser's coherence length is less than the thickness of the bulk. In this case, the sum is incoherent with the expressions for T and R given by:

$$R = R_F + R_F T_F^2 T_{\text{bulk}}^2 \sum_{m=0}^N [R_F T_{\text{bulk}}]^{2m} \quad (1.5)$$

$$T = T_F^2 T_{\text{bulk}} \sum_{m=0}^N [R_F T_{\text{bulk}}]^{2m}$$

For the case of an infinite number of bounces, Eq. (1.5) simplifies to:

$$R = R_F + \frac{R_F T_F^2 T_{\text{bulk}}^2}{1 - R_F^2 T_{\text{bulk}}^2} \quad (1.6)$$

$$T = \frac{T_F^2 T_{\text{bulk}}}{1 - R_F^2 T_{\text{bulk}}^2},$$

whereas if only a single bounce occurs, Eq. (1.5) reduces to:

$$R = R_F + R_F T_F^2 T_{\text{bulk}}^2 \quad (1.7)$$

$$T = T_F^2 T_{\text{bulk}}$$

We now consider the fractional error introduced by ignoring the interface effects de-

scribed by T_F and R_F . That is, what would happen if we assume that the interfaces have no effect on the transmitted intensity? We introduce the relative error ϵ made by ignoring the Fresnel coefficients of Eq. (1.6):

$$\epsilon \equiv \frac{T_{\text{bulk}}}{T} - 1 \quad (1.8)$$

As an example, consider a 100 nm thick Si sample measured in transmission near the Si *L*-edge (about 100 eV), as shown in Fig. 1.4. The relative error is in the range of one part in 10^4 to 10^5 , well below our experimental detection limit. Silicon was chosen due to its data availability above and below the absorption edge, but this behavior is true for all materials in normal transmission.

The real part of the complex index becomes important when the sample isn't normal to the beam, as shown in the right panel of Fig. 1.3. In this case, the Fresnel equations are a bit messier:

$$\begin{aligned} R_s &= \left| \frac{\tilde{n}_1 \cos \theta_i - \tilde{n}_2 \cos \theta_t}{\tilde{n}_1 \cos \theta_i + \tilde{n}_2 \cos \theta_t} \right|^2 \\ R_p &= \left| \frac{\tilde{n}_1 \cos \theta_t - \tilde{n}_2 \cos \theta_i}{\tilde{n}_1 \cos \theta_t + \tilde{n}_2 \cos \theta_i} \right|^2 \end{aligned} \quad (1.9)$$

$$T_s = 1 - R_s$$

$$T_p = 1 - R_p$$

Here, the subscripts s and p denote the polarization relative to the surface normal. In a vacuum, $\tilde{n}_1 = 1$ and \tilde{n}_2 is the index of the sample. We can extract the relevant physics without any additional manipulation of the Eq. (1.9). Right away, we can see that unlike Eq. (1.2), Eq. (1.9) is symmetric in the real and imaginary parts of the sample's complex index, \tilde{n}_2 . In the limit of a thick slab, ($h \gg \alpha$), the light is attenuated before it can reflect off the back surface and we have $T \rightarrow 0$ and $R \rightarrow R_{s,p}$. That is, the only contributions to the reflected intensity are from the interface and possibly the sample volume within $z \approx 1/\alpha$ of the interface. As a result, both parts of \tilde{n}_2 will make significant contributions to the reflected intensity.

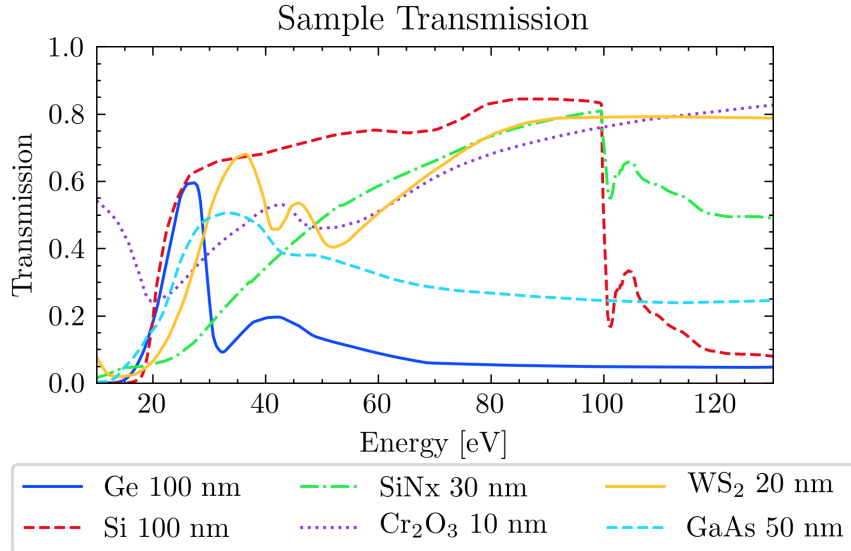


Figure 1.5: Calculated XUV transmission of various materials. Data from [6].

1.4 Sample Requirements and Geometry

There are several sample requirements for a successful condensed matter transient absorption experiment. First and foremost, the sample needs to have an absorption edge within the bandwidth of the XUV source. Second, the material must be the correct thickness for a transmission measurement, given the capabilities of the XUV light source and detector. If the material is too thick, the ground state will absorb most of the XUV flux and the resulting spectrum will be too close to the noise floor of the apparatus. If it is too thin, the laser-induced change of the ground state (on the order of 1 – 10%) will be lost in the noise. As a general guideline, a sample that absorbs 50% at the spectral feature of interest provides a good compromise between these conflicting requirements. Fig. 1.5 plots the expected transmission of several materials, calculated from the atomic scattering factors [6]. A typical sample will be on the order of 10 - 200 nm thick, depending on the material.

Another upper bound for sample thickness comes from material dispersion. In any material, the XUV light ($n_{\text{IR}} \sim 1$) will outpace the IR light ($n_{\text{IR}} > 1$). This effect can be significant even for ultrathin films. In order to keep the phase slippage between the XUV and IR light below half an IR period, the sample thickness h must obey the following

relationship:

$$h \leq \frac{1}{2} \frac{\lambda_{\text{IR}}}{n_{\text{IR}} - n_{\text{XUV}}} \quad (1.10)$$

For germanium excited with $\lambda_{\text{IR}} = 1430$ nm and probed with 30 eV XUV at the $M_{4,5}$ edge, $n_{\text{IR}} = 4.2481$ [12] and $n_{\text{XUV}} = 0.992536$ [6], which gives a maximum thickness of 220 nm.

Next, the sample needs to be excitable using laser sources present in our lab (i.e., ultrafast pulses with wavelengths between 800 nm and a couple of microns). To minimize the slow build up of heat (on the order of seconds) and laser-induced damage, the sample needs to be rastered through the laser focus as the experiment is performed. This rastering method necessitates both a large clear aperture ($\sim 1 \text{ mm}^2 - 1 \text{ cm}^2$) and good sample uniformity. Samples that meet the above thickness and clear aperture requirements are extremely delicate, with thicknesses between 5,000 and 100,000 times smaller than their freestanding lateral dimensions. As such, one should expect most samples to break before, during and after measurements, and a successful experiment will have a materials pipeline that is capable of producing multiple, consistent samples in a short time frame.

1.5 Absorbance and Transient Absorbance Data Collection Methods

The *absorbance*¹ A is defined as the negative logarithm of the transmission T :

$$A(E) = -\log_{10}(T) = -\log_{10}\left(\frac{S_{gs}(E)}{S_{vac}(E)}\right). \quad (1.11)$$

In Eq. (1.11), $S_{gs}(E)$ is the XUV spectrum transmitted by the sample in its ground state and $S_{vac}(E)$ is the spectrum without the sample present. Therefore we can measure the sample's ground state absorbance by measuring the harmonic spectrum with and without the sample in the XUV beam.

The *change in absorbance* ΔA between the ground and excited state which is induced

¹The terms absorbance and optical density are often used interchangably.

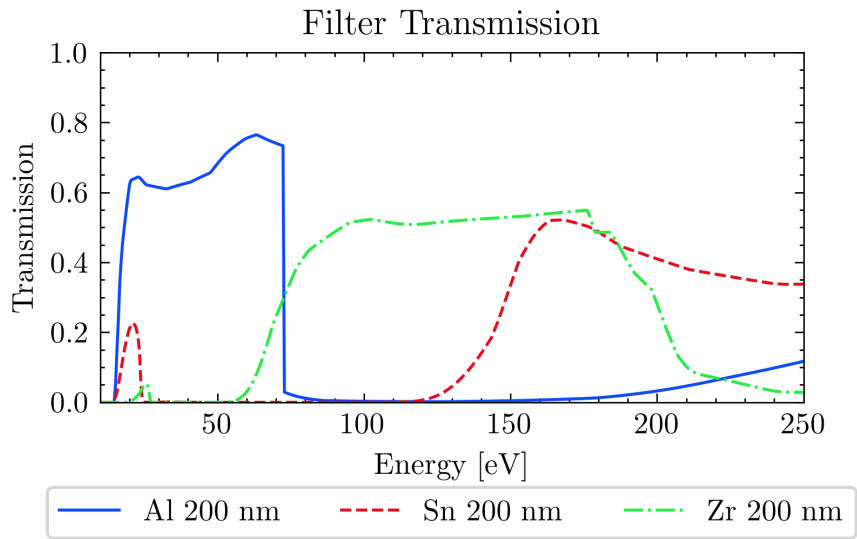


Figure 1.6: Calculated XUV transmission of various metallic filters. Data from [6].

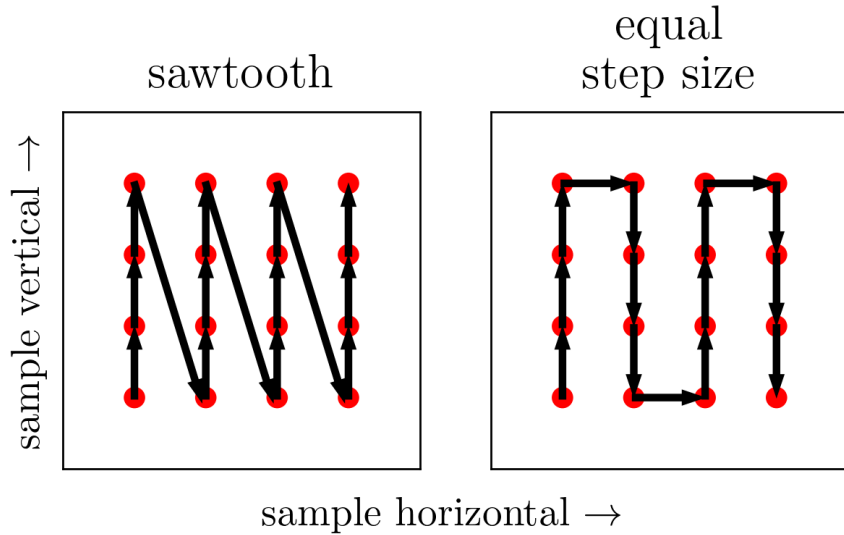


Figure 1.7: Schematic of competing raster methods, shown in the sample's reference frame. The clear aperture of the sample is represented by the interior of the black square. The laser propagation direction is out of the page. The laser focal spots are shown as red circles, and the movement of the sample holder relative to the laser focus is indicated by arrows. This diagram is to scale for a $1 \times 1 \text{ mm}^2$ clear aperture sample, a $60 \mu\text{m}$ diameter IR focal spot and a $200 \mu\text{m}$ step size.

by an IR pulse is therefore:

$$\begin{aligned}\Delta A(E, \tau) &= A_{\text{sig}}(E, \tau) - A_{\text{gs}}(E) \\ &= -\log_{10} \left(\frac{S_{\text{sig}}(E, \tau)}{S_{\text{vac}}(E)} \right) - \log_{10} \left(\frac{S_{\text{gs}}(E)}{S_{\text{vac}}(E)} \right) \\ &= -\log_{10} \left(\frac{S_{\text{sig}}(E, \tau)}{S_{\text{gs}}(E)} \right).\end{aligned}\quad (1.12)$$

In Eq. (1.12), the signal spectrum $S_{\text{sig}}(E, \tau)$ is the spectra that results from an IR pulse hitting the sample, followed by an XUV pulse after a delay of $\tau \equiv t_{\text{XUV}} - t_{\text{IR}}$. Note that negative delays mean the XUV arrives at the sample before the IR and zero delay indicates temporal overlap of the two pulses. It is assumed that a delay of negative infinity is equivalent to a ground state measurement: $S_{\text{sig}}(E, \tau = -\infty) = S_{\text{gs}}$.

An ATAS experiment is simply a collection of recorded spectra taken over a range of delay points with otherwise identical experimental conditions. However, we have implemented several techniques to improve the fidelity of our data.

HHG is an extremely inefficient process, with a IR to XUV conversion ratio on the order of 10^{-6} . After the generation cell, the leftover IR light must be blocked or it will destroy any sample located downstream. We use a thin metallic filter (Al, Zr or Sn), placed about 1 m after the harmonic source, to strip out the generating infrared field. The choice of filter is dictated by the photon energy range of the spectral features we want to study. For more detail, see Fig. 1.6.

As an extremely nonlinear process, HHG's conversion efficiency is highly dependent on the input laser pointing, peak power, pulse duration, spatial mode, etc. – all of which are affected by laboratory environmental conditions and the activity of other group members within our lab complex. As a result, even during “ideal” experimental conditions, the total harmonic yield drifts slowly throughout the course of the experiment. To minimize the effect of this slow drift, we take a ground state spectrum for each delay point. A computer-controlled home-built shutter system blocks the IR laser in the pump arm between measurements (see Fig. 1.1). Taking back-to-back ground and excited state spectra significantly lowers the harmonic stability requirements; we require stability on the order of

twice the exposure time (several seconds), rather than the entire experimental run (several hours).

Our spectrometer's CMOS camera has a bit depth of 16, corresponding to a maximum value of $2^{16} - 1 = 65,535$ counts before saturation. The exposure time is set so that the amplitude of the brightest harmonic on the detector is about 10% below this limit, which allows for an upward drift in harmonic yield to occur without invalidating the dataset. An exposure time of 3 seconds is typical for a 200 nm Al filter with a 100 nm Ge sample at 125 Hz (375 laser shots), an MCP voltage of 2200 VDC, and 2×2 camera pixel binning.

Although the Spitfire laser system has a maximum repetition rate of 1 kHz, we perform solid state ATAS experiments at a much lower rate (125 or 250 Hz) by adjusting amplifier's Pockels cell firing rate. The lower repetition rate allows the sample to more fully relax between laser shots, reducing the effects of millisecond thermal processes on our measurements. It also reduces the average power on the sample for a given pulse energy, which lowers the steady state temperature of the sample. On the other hand, it allows us to increase the pulse energy while maintaining a constant average power on the sample.

During the experiment, the sample is rastered across the focus to reduce any deleterious effects of long term uninterrupted laser exposure. During motor movement, the IR beam is blocked with a shutter but the relatively weak XUV beam is allowed to remain on the sample. Each pair of measurements (ground state, excited state) in a given delay scan has a unique position on the sample. Typical step sizes are 200 μm , which is larger than the measured XUV spot size of $\sim 12 \mu\text{m}$ and the IR spot size of $\sim 30 \mu\text{m}$. Two raster schemes are schematically shown in Fig. 1.7. The method shown in the left panel produces a sawtooth pattern on the sample. This method gives very accurate positioning, as the vertical motor is almost always approaching the final position from the same direction. However, the diagonal steps are $\sqrt{N^2 + 1}$ times longer than the vertical steps, where N is the number of vertical steps in the pattern. As a result, there is a bimodal distribution of motor transit times between measurements. If the sample is not fully relaxed between motor movements, this will lead to an inconsistent measurement of the ground state $S_{gs}(E)$. The method shown in the right panel alleviates this problem by requiring equal step sizes.

Measurements presented in this work were acquired using the method shown in the right panel.

Before measuring a sample’s response for the first time, or after a major optical alignment, an XUV transmission map of the sample must be created. Creating this map serves two purposes: it verifies sample XUV absorption uniformity and it determines the motor coordinates of the sample’s clear aperture. To avoid edge effects, the edges of the raster area are chosen to be 200 μm away from the edge of the clear aperture (see Fig. 1.7).

The next step is a measurement of the absorbance (A) of the ground state of the sample. Per Eq. (1.11), this is achieved by taking spectra with (S_{gs}) and without (S_{vac}) the sample in the XUV beam. These measurements are taken back-to-back (as quickly as the motors will allow, <10 seconds between spectra) to minimize harmonic amplitude drift between measurements. Note that because we do not have a simultaneous harmonic amplitude reference measurement, a change in the XUV input flux during this measurement can manifest itself as a change in the absorbance. A typical ground state measurement of a 100 nm Ge sample is shown in Fig. 1.12.

The transient data collection sequence can be summarized as *excited state \rightarrow ground state \rightarrow move motors*. Details of this sequence are as follows. First, the sample moves to a given raster position and delay wedge position, the IR shutter opens and an excited state spectrum $S_{\text{sig}}(\tau, E)$ is recorded. Then, the IR shutter closes and a ground state spectrum $S_{\text{gs}}(E)$ is recorded. To minimize the duration of the experiment, an XUV reference spectrum $S_{\text{vac}}(E)$ is not recorded. Finally, the sample moves to the next raster position as the delay wedge pair moves to the next delay position. The system is programmed to wait for the wedges to become stationary before the next measurement begins.

Note that in this sequence, the time between the i^{th} excited state and i^{th} ground state measurements is equal to the exposure time, but the time between the i^{th} ground state measurement and the $(i+1)^{\text{th}}$ excited state measurement is equal to the delay wedge motor transit time². This sequence is preferable to the alternative (*ground state \rightarrow excited state \rightarrow*

²In this analysis we neglect the role of the XUV-IR delay τ . However, $\tau \sim 1 \text{ fs} - 1 \text{ ps}$, which is negligible compared to the motor transit time $\sim 1 \text{ s}$.

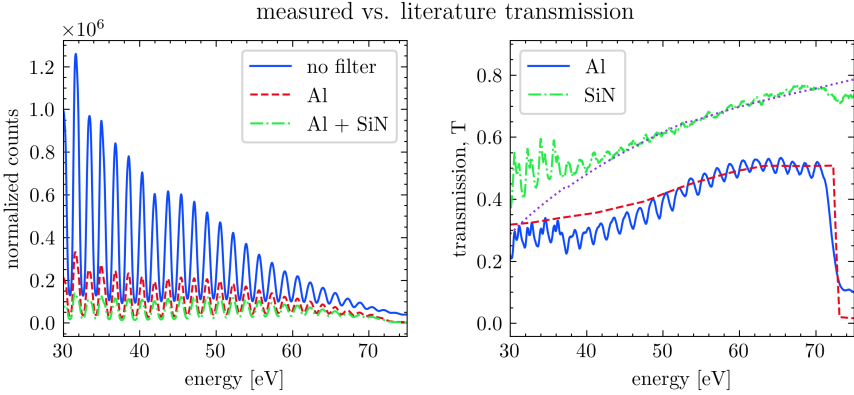


Figure 1.8: XUV transmission measurements of Al metallic filter and silicon nitride membrane. Left panel: normalized XUV counts for i) unfiltered HHG signal, ii) HHG going through a 200 nm Al filter and iii) HHG going through a 200 nm Al filter and 30 nm of silicon nitride. Counts are scaled by the Jacobian (Eq. (1.27)). Right panel: transmission curves obtained from the left panel’s data. Also shown are literature values for 20 nm of silicon nitride and 200 nm of Al with two 4 nm oxide layers [6]. Multilayer interference is not taken into account. Oscillations in measured transmission are numerical artifacts which will be discussed in the text.

move motors), as that would result in a delay step size-dependent relaxation time between the i^{th} excited state and the $i+1^{th}$ ground state measurement. Since $\Delta A(E, \tau)$ is calculated between pairs of ground and excited state measurements at a given delay wedge position, the sequence *excited state \rightarrow ground state \rightarrow move motors* is preferred.

To further improve our signal to noise ratio, we average multiple delay scans together. A typical ΔA measurement will be repeated between 10 and 50 times. Each delay scan uses the raster points of the previous delay scan so there is a one-to-one mapping of delay to sample position.

1.6 The Supporting Nitride Membrane

While most materials have an absorption edge within the range 25 - 150 eV, there are very few commercially available pre-fabricated materials with both the requisite large clear aperture and thickness. Note that either characteristic is relatively easy to achieve individually, but their combination presents unique materials challenges. We considered three synthesis methods to produce this quasi-2D sample:

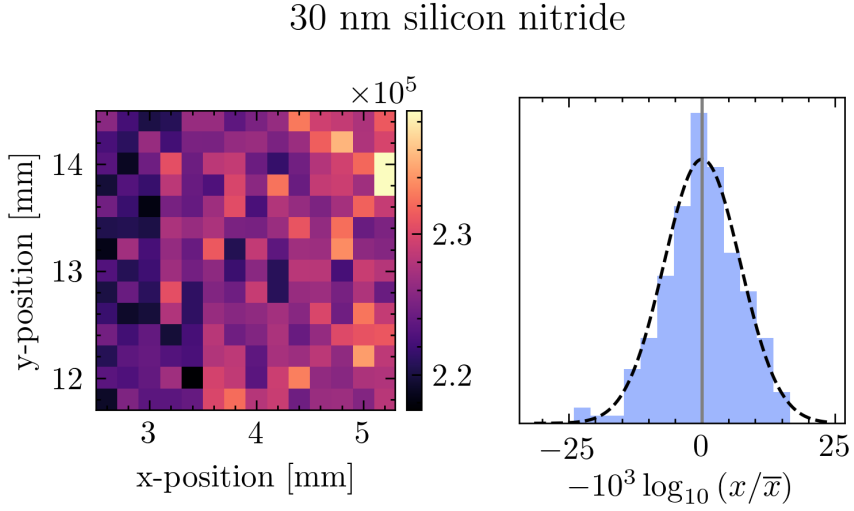


Figure 1.9: XUV transmission map of 30 nm silicone nitride freestanding membrane. Left panel: integrated harmonic peaks in the range ?? – ?? eV. Sample holder motor positions are indicated by x- and y-positions. Right panel: histogram of logarithmic deviation of counts from the average. Dashed line shows a normal distribution.

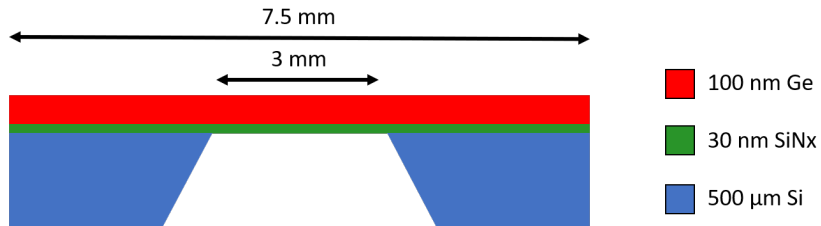


Figure 1.10: Cartoon showing the cross section of the free standing sample heterostructure. A 500 μ m thick Si frame supports a freestanding 30 nm low stress silicon nitride membrane (Norcada QX7300X), upon which 100 nm of germanium has been deposited. The Si frame has a 3x3 mm² square clear aperture and a 7.5x7.5 mm² square external dimension. The taper of the Si frame thickness along the perimeter of the clear aperture forms a knife edge. In an ATAS experiment, the XUV and IR pulses propagate from the top to bottom of the figure.

1. sample growth on a traditional substrate, followed by chemical back-etching or milling of the substrate until sub-micron thickness of the heterostructure is achieved;
2. sample growth on a traditional substrate, followed by mechanical transfer onto a membrane;
3. sample growth on a membrane.

Sample quality and composition is heavily impacted by local growth conditions such as substrate temperature, deposition rate, substrate crystal cut, substrate-sample lattice mismatch, etc. Many of these characteristics are changed when growing on a substrate of a different cut, or by replacing a substrate with a membrane. In general, one should not expect success when applying a substrate-optimized growth recipe to a freestanding membrane. Therefore, methods 1 and 2 will yield the highest quality samples, as they leverage already-developed sample recipes. However, both methods require a technically difficult second step that is prone to failure.

Selective chemical etching recipes exist for certain compounds, but they usually require an additional layer in the heterostructure to protect the sample. Adding this layer will come at the expense of the total XUV flux transmitted by the heterostructure. Additionally, the chemical etching rates are highly dependent on local chemistry, fluid convection and temperature [3], which ultimately means that the amount of material removed is uncontrollable and unrepeatable within our requirements ($499.9 \mu\text{m} \pm 10 \text{ nm}$ removed from a $500 \mu\text{m}$ substrate). For these reasons, we decided to not pursue a chemical etch recipe. Ion or electron milling is more controllable, but too expensive to implement on a large scale. The above reasons preclude the use of Method 1.

Mechanical transfer of thin samples is a tried and true method, but it usually results in flakes with lateral dimensions on the order of $100 \mu\text{m}$. Repeated transfer of many flakes is possible, but there little control over their exact positioning on the membrane. This results in folded or overlapping flakes. These mishaps increase the effective optical density of the sample, changing the IR and XUV absorption properties significantly.

An XUV spatial measurement needs to be taken prior to any ATAS experiment, but a

non-uniform distribution of flakes on a membrane would require a much higher resolution map. This is because the flakes are on the order of the XUV and IR focii, so it is critical that the raster points in Fig. 1.7 correspond to the center of each flake to avoid edge diffraction and to minimize the effects of slow laser pointing drift. For a uniform film, a map can be taken using $200\text{--}250 \mu\text{m}$ step sizes, as the most important feature is the border of the clear aperture. On the other hand, each flake would have to be sampled ~ 5 times in each direction to find its center. As a conservative estimate, a membrane covered with $100 \times 100 \mu\text{m}^2$ flakes would require a step size of $20 \mu\text{m}$, which increases the number of raster points by a factor of $10^2 = 100$. Considering that a $3 \times 3 \text{ mm}^2$ clear aperture sampled with $200 \mu\text{m}$ steps takes ~ 45 minutes to map, a random distribution of flakes would take a prohibitively long time to map out.

With the first two methods ruled out, we turn to the third method of growing directly on a freestanding membrane. Although it will result in a lower quality sample, it does not have the same technical hurdles of the previous two methods. However, the large clear area makes the heterostructure extremely fragile. We initially attempted to circumvent this problem by using smaller clear apertures.

As shown in Fig. 1.7, most of the sample's area isn't directly used by the laser - it exists as a buffer between the grid of sample points. An alternative to a single clear aperture is an array of micro-apertures, each with a diameter on the order of the IR spot size. The micro-apertures exist within a mechanically robust substrate and a thin membrane lies on top of the structure. This configuration significantly eases the material strength requirements by reducing the size of the unsupported area from cm-scale to sub-mm-scale. The regular grid of apertures avoids the difficulties of a randomly distributed sample, easing the XUV mapping step size requirements. Fortunately, these arrays are commercially available from Silson, Norcada (silicon nitride membranes) and US Applied Diamond (diamond membranes) but we encountered technical difficulties in their implementation. Because the aperture size is on the order of the size of the IR focal spot, there is very little room for positioning error, and our motors were insufficiently precise for this application. Further, these arrays are typically only available in at most a 3×3 array, which provides an insufficient number of

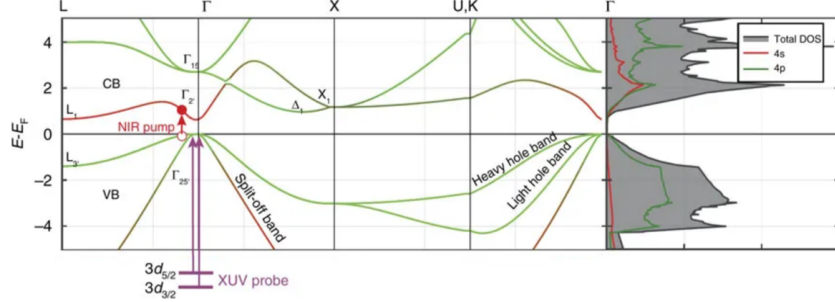


Figure 1.11: Band structure and orbital character of germanium. Purple arrows indicate XUV-induced transitions from the $3d$ core levels to the valence bands. Red arrow indicates IR-induced transition across the direct band gap. Figure adapted from [16].

raster points for an ATAS experiment.

With these limitations in mind, we decided to use large aperture x-ray windows from Norcada. These windows consist of a mechanically robust Si frame substrate with a square clear aperture cut through the center. The structure is fabricated so that a thin membrane covers the clear aperture. A schematic of the cross section is shown in Fig. 1.10.

Norcada offers these structures with either a silicon (polycrystalline or single-crystal) or a silicon nitride membrane. An ideal membrane is transparent to both XUV and IR wavelengths with a high damage threshold. Referring to Fig. 1.5, 100 nm of Si provides a relatively flat transmission curve from 25 to 100 eV. In contrast, 30 nm of silicon nitride has poor, but featureless, transmission at lower energies. Both materials transmit light below their bandgaps (5 eV for SiN and 1.14 eV for Si). Finally, silicon nitride's higher bandgap results in a significantly higher laser damage threshold [2, 5, 9]. Taking all these factors into account, we decided to use 30 nm silicon nitride membranes for germanium transient absorption experiments. The measured transmission of a typical membrane is shown in Fig. 1.8.

1.7 The Germanium Sample

Germanium is a technologically important semiconductor with an indirect bandgap of 0.66 eV (1880 nm) and a direct gap of 0.8 eV (1550 nm). Its small band gap allows for single-

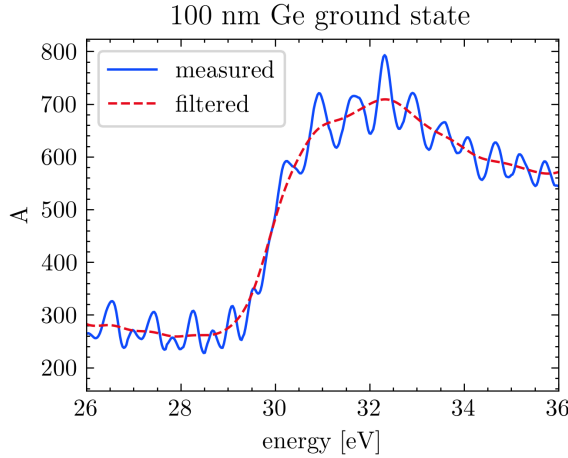


Figure 1.12: Measured ground absorbance A of a 100 nm Ge film on a 30 nm silicon nitride membrane. The contribution of the membrane has been subtracted. Blue line is the measured absorbance A . The red dashed line shows the result of numerical filtering to eliminate numerical artifacts (described in main text).

photon excitation using the signal output of our TOPAS.

The band structure of Ge is shown in Fig. 1.11. DFT calculations [16] indicate that the valence band has primarily $4p$ orbital character, and the conduction band has equal parts $4s$ and $4p$ character. However, the orbital character of the conduction band in the Γ valley is primarily $4s$.

The $M_{4,5}$ edge in germanium is near 30 eV, which corresponds to a transition between both the $3d_{5/2}$ (29.3 eV) and $3d_{3/2}$ (29.9 eV) states to the valence states near Fermi level. The ground state absorbance of germanium as measured with the TABLE apparatus, is shown in Fig. 1.12. The M edge easily visible in the measured data, with the absorbance more than doubling across the edge.

The transition $3d \rightarrow 4s$ is forbidden from the dipole selection rules, but $3d \rightarrow 4p$ is allowed. Therefore, the XUV primarily probes the valence band in the Γ valley. This is depicted in Fig. 1.12 as purple arrows. IR light with a photon energy exceeding the bandgap will promote electrons across the direct bandgap, which is indicated as a red arrow in Fig. 1.12, leaving behind a hole in the valence band.

Germanium is a good sample for a number of reasons. First, it has an XUV absorption

feature at a relatively low photon energy, where we have bright XUV flux. We are able to tune our generation conditions to optimize this part of the XUV spectrum while simultaneously suppressing the generation of photons at higher energies which can skew the results. Second, we can access the bandgap using the signal output of our TOPAS. Finally, its simple chemistry means that samples can be grown in quantity using simple electron beam deposition techniques.

Ultrafast dynamics in germanium have previously been studied using few-cycle VIS-NIR light (800 nm) in both transmission [16, 17] and reflection geometries [8]. However, the ultrafast dynamics of this material have not been studied using longer wavelength excitation. To this end, approximately 100 nm of germanium was deposited onto a 30 nm silicon nitride membrane using electron beam deposition (Kurt J. Lesker Lab 18) in the NanoSystem's Laboratory.

1.8 IR Pump Arm Considerations

In a condensed matter ATAS measurement, the IR intensity is usually set to be as high as possible (while avoiding sample damage) to maximize the sample's transient response. Under these conditions, $\sim 1\%$ of valence electrons are excited across the bandgap by the laser [4, 13, 16]. Calculations were performed to estimate the input laser power necessary to achieve the appropriate excitation fraction, but ultimately the input power needs to be determined experimentally through trial and error. Note that many of these calculations are linear with respect to input pulse energy, so we assume a 1 μJ pulse and scale the results at the end.

1.8.1 Calculation of IR Intensity at Focus

The profile of the TOPAS output at $\lambda=1500$ nm was measured immediately before diverging lens L4 using an Electrophysics PV320 thermal camera. The beam was propagated numerically using the Python package *Lightpipes for Python* [14] through the remainder of the pump arm towards the focus using a grid size of $2^{13} \times 2^{13}$. The result of this calculation

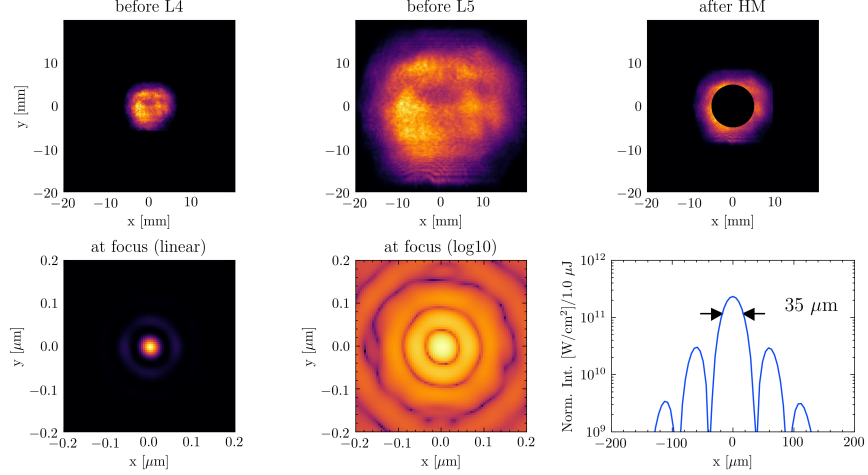


Figure 1.13: Numerical propagation of the IR ($\lambda=1500$ nm) beam through the pump arm. Beam path layout follows Fig. 1.1. Each panel shows the intensity of the beam as the beam propagates towards the focus. The first panel shows the measured intensity (Electrophysics PV320 thermal camera), all other panels are calculations. The arrows on the lineout indicate FWHM. All calculations are for vacuum ($n=1$). See text for details.

is shown in Fig. 1.13. Optical element parameters are as follows: L5 is a $f = +500$ mm Thorlabs LA1380-C, located 68.5 cm after L4 ($f = -300$ mm, Thorlabs LF1015-C). The hole mirror HM is located 53 cm after L5 and has an inner radius of 5 mm. Clear apertures of 22.86 mm (L4), 45.72 mm (L5) and 50.8 mm (HM) were assumed. A 65 fs Gaussian temporal profile containing 1 μJ of energy was assumed.

Reflection losses from the 2 Ag mirrors, 2 AR-coated lenses and uncoated CaF₂ vacuum window are responsible for a 26.2% reduction in transmitted power. Additionally, the geometry of the hole mirror causes only 56% of incident power to be incident on a reflective surface (the rest is lost to the central aperture). In total, the pump arm transmits 41.3% of the power from before L4 to the focus.

The IR intensity makes an Airy-like diffraction pattern at the focal plane. There is an intense bright spot surrounded by a series of rings, with the intensity of each ring as the distance from the center increases. The rings exhibit a periodic modulation in intensity with respect to angle ϕ . This four-fold symmetry is due to the square-like spatial profile of the TOPAS output, whereas the clipping from the hole mirror's aperture is responsible for the

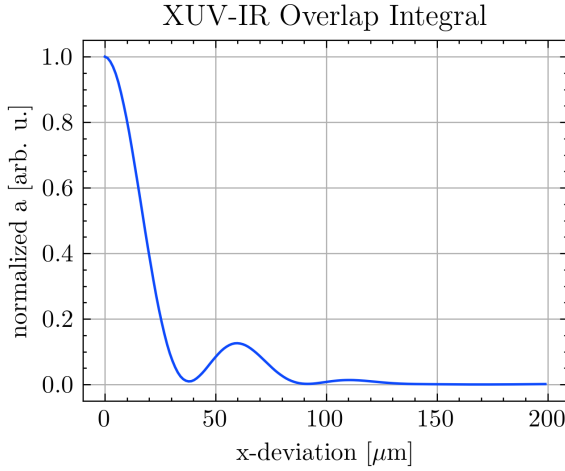


Figure 1.14: XUV-IR overlap function, as defined in Eq. (1.19), calculated using the numerical simulation results of Fig. 1.13 and a Gaussian XUV beam with a $6\text{ }\mu\text{m}$ waist. The result has been normalized to perfect overlap. **NOTE: change the y-axis label to something like a/a_{max} , and the x-axis label to x_0 .**

central peak and ring structure. The central lobe has a peak intensity of $\sim 2.3 \times 10^{11}\text{ W/cm}^2$ per $1\text{ }\mu\text{J}$ input pulse energy and a FWHM of $35\text{ }\mu\text{m}$. The first ring has a radius of $59\text{ }\mu\text{m}$ and a peak intensity $\sim 2.9 \times 10^{10}\text{ W/cm}^2$ per input μJ pulse energy. Thus the central lobe's peak intensity is about an order of magnitude larger than the ring's intensity. However, the central spot only contains about 49% of the total power, as the rings cover a much larger area.

Note that the above calculations assume perfect alignment into the hole mirror (i.e., the IR beam is centered on the central aperture of the hole mirror). If the IR beam is misaligned to the hole mirror, then the transmission to the focus will increase as the most intense part of the beam is no longer clipped by the central aperture. Therefore, a drift in the laser's pointing during an experiment can effect the sample's interaction intensity.

1.8.2 Estimation of Excited Carrier Density

We are concerned with two quantities: the peak excitation fraction in the sample and the average excitation fraction at the location of the XUV focus. The former quantity is relevant when considering sample damage, whereas the latter will be proportional to the measured

signal. If the XUV and IR spots are perfectly overlapped at the sample plane, then these two quantities are equal. We first calculate the peak excitation fraction, then we consider how a misaligned beam will effect the measured signal.

The electric field inside the sample E_{int} is related to the external electric field by the following equation [13]:

$$E_{\text{int}} = \frac{2}{1 + \sqrt{\epsilon}} E_{\text{ext}} \quad (1.13)$$

where E_{int} is the electric field inside the sample, E_{ext} is the electric field outside the sample, ϵ is the dielectric constant and its square root is the refractive index n_{IR} . The internal intensity I_{int} is the square of the internal electric field. For germanium at $\lambda = 1430$ nm, $n_{\text{IR}} = 4.2481$, and we have the following relations:

$$\begin{aligned} E_{\text{int}} &= 0.381 \times E_{\text{ext}} \\ I_{\text{int}} &= 0.145 \times I_{\text{ext}} \end{aligned} \quad (1.14)$$

Given our laser parameters, we can estimate the highest carrier density within the sample. First, we estimate the absorbed laser fluence, F_{abs} [7]:

$$F_{\text{abs}} = F_{\text{inc}} (1 - R) (1 - \exp(-\alpha L)) (1 + R \exp(-\alpha L)), \quad (1.15)$$

where F_{inc} is the incident fluence, R is the reflectivity equal to the square of the Fresnel coefficient, α is the absorption coefficient and L is the sample thickness. The bracketed terms in Eq. (1.15) are the fraction of fluence transmitted by the first surface, the fraction absorbed by a single pass through the sample, and the additional absorption due to a back reflection off the rear face of the sample. Note that the back-propagating beam will arrive (on average) at a delay of $n_{\text{IR}}L/(2c) \approx 0.7$ fs later than the forward-propagating beam. This time scale is nearly two order of magnitude less than the pulse duration, so we should expect any electron dynamics initiated by the back reflection to contribute to the measured signal.

If each absorbed photon corresponds to an excited electron, then the excited carrier

density ΔN is given by the following expression [4]:

$$\Delta N = \frac{F_{\text{abs}}}{\hbar\omega} \frac{1}{L}, \quad (1.16)$$

where $\hbar\omega$ is the IR photon energy. In Eq. (1.16), the quantity $F_{\text{abs}}/(\hbar\omega)$ represents the number of absorbed photons per unit area; dividing this quantity by the sample thickness gives the number of absorbed photons per unit volume. This assumes that the skin depth of the material is greater than membrane thickness.

Finally, we convert the excited carrier density to a fractional excitation. Germanium has $N_{\text{u.c.}} = 2$ valence electrons per unit cell, and each unit cell has a volume $V_{\text{u.c.}} = 4.527 \times 10^{-23} \text{ cm}^3$. Therefore the fractional carrier excitation is

$$f = \Delta N \frac{V_{\text{u.c.}}}{N_{\text{u.c.}}} \quad (1.17)$$

We can use literature values for 100 nm of germanium pumped at $\lambda = 1430 \text{ nm}$ light. From the literature [12], $R = 0.38315$, $\alpha = 5803.4 \text{ cm}^{-1}$, and so $F_{\text{abs}} = 0.0413 \times F_{\text{inc}}$. Therefore, only about 4.13% of the incident fluence is absorbed by the sample.

According to the calculations in Fig. 1.13, for each $1 \mu\text{J}$ energy input pulse (measured at L4), $0.413 \mu\text{J}$ makes it to the focal plane. 49% of that energy is within the main lobe, which contains $0.202 \mu\text{J}$ of energy. Approximating the central lobe as a Gaussian beam with a FWHM of $35 \mu\text{m}$ and a pulse energy of $0.202 \mu\text{J}$, the peak fluence is calculated by dividing the total energy of the Gaussian by $\pi w^2/2$. The Gaussian beam waist w is related to the FWHM via $w^2 = \text{FWHM}^2/(2 \ln 2)$. Thus, for each $1 \mu\text{J}$ input energy, the peak fluence in the central lobe is 14.6 mJ/cm^2 and the absorbed peak fluence is 0.60 mJ/cm^2 . This corresponds to an peak excited carrier density of $4.3 \times 10^{20} \text{ cm}^{-3}$ and an excitation fraction of 0.98% (per $1 \mu\text{J}$ of input energy).

1.8.3 The XUV-IR Overlap Integral

The excitation fraction can be computed for each spatial coordinate on the sample using the above method and the predicted intensity distribution from the numerical beam propagation calculations. Because the electrons are being excited via a single-photon process, the excited

carrier density will be proportional to the fluence, and thus proportional to the intensity shown in Fig. 1.13. Because the intensity of the XUV is very weak, the absorption of the XUV by the sample is also linear. Thus, we should expect the ATAS signal to be proportional to the XUV-IR overlap integral:

$$a = \frac{\int dV I_{\text{IR}} I_{\text{XUV}}}{\int dV I_{\text{IR}} \int dV I_{\text{XUV}}} \quad (1.18)$$

Here, the integration volume is over the entire sample. If we assume that the intensity distribution does not appreciably change over the thickness of the sample, we can simplify the above equation. This is a reasonable assumption because the sample ($L = 100$ nm) is much thinner than the Rayleigh range ($z_R \sim 1$ mm), and the absorption is low ($\sim 4\%$). So we assume the sample is a δ -function in thickness and only evaluate the intensities at the focal plane. With this assumption, the overlap integral becomes:

$$a = L \frac{\int dA I_{\text{IR}} I_{\text{XUV}}}{\int dA I_{\text{IR}} \int dA I_{\text{XUV}}} \quad (1.19)$$

Knife edge measurements have been performed on the XUV light, showing that it has a Gaussian spatial profile with a beam waist of $6 \mu\text{m}$. We write down the spatial profile of the XUV light at the focus:

$$I^{\text{XUV}} = I_0^{\text{XUV}} \exp(-2((x - x_0)^2 + (y - y_0)^2)/w_{\text{XUV}}^2) \quad (1.20)$$

Here, I_0^{XUV} is the peak intensity and w_{XUV} is the beam waist (radius), defined as the point where the intensity falls to $e^{-2} = 13.5\%$ of its maximum. The lateral shift from the center of the IR focal spot in the horizontal and vertical directions is x_0 and y_0 , respectively. With this formulation, and using the simulation results for the IR spot, the XUV-IR overlap integral is calculated as a function of XUV-IR misalignment (x_0, y_0). This result is shown in Fig. 1.14. Here, XUV beam is translated relative to the IR beam in the horizontal direction (x_0) and the overlap is computed from Eq. (1.19).

Fig. 1.14 shows the sensitivity of a condensed matter ATAS experiment to relative alignment.³ A spatial overlap deviation of $10 \mu\text{m}$ will cause the XUV-IR overlap - and

³Note that the relevant parameter in Eq. (1.19) is the relative positions of the two focal spots. We have

thus the measured signal - to drop by 20%. Note that a $10 \mu\text{m}$ displacement of the IR at the sample corresponds to a $15 \mu\text{rad}$ tilting of the hole mirror (HM). There are two ways misalignment can affect experimental results. If the relative positions of the XUV and IR focal spots changes as an experiment is performed, then the recorded ATAS signal would be a function of both the laser-induced dynamics and the XUV-IR spatial misalignment. On the other hand, if the entire experiment is performed using a constant misalignment, we would be exciting the sample to some peak excitation fraction f , but our probe would be measuring a lower excitation fraction ($\approx fa/a_{max}$). Consequently, the measured ATAS signal would be lower than otherwise expected, and any attempts to boost the signal by increasing the interaction intensity could result in permanent laser-induced sample damage.

A condensed matter ATAS experiment has much tighter alignment tolerances than a gas phase experiment. This discrepancy is a simple consequence of sample geometry and density. In either experiment, the measured signal comes from the region of space where the sample density, XUV intensity and IR intensity overlap. The transmission of XUV through the sample is, to first order, $T = \exp(-n\mu_a d)$, where n is the number density, d is the sample thickness and μ_a is the photoabsorption cross section. As discussed above, for technical reasons the experiment should be designed with $T \approx 1/2$. Therefore, the product $n\mu_a d$ will be approximately constant for any transient absorption experiment.

The number density of a condensed phase sample is determined by the chemistry of the compound and is on the order of $4 \times 10^{22} \text{ atoms/cm}^3$. The experimentalist is free to engineer clever sample geometries, heterostructures and/or nanopatterns, but the high atomic density (and thus absorption coefficient) dictates a total sample thickness on the order of 100 nm. On the other hand, the spatial profile and density of a gas phase sample is determined by the gas nozzle design and its backing pressure, respectively. A typical nozzle used in our lab produces a gas plume with lateral dimensions on the order of 200 - 500 μm . This effectively creates a sample that is three orders of magnitude thicker than a condensed phase sample, which relaxes the alignment constraints significantly. This has important consequences for the alignment of the sample.

yet to calculate the sensitivity of spatial overlap to deviations in the input laser pointing.

If the XUV and IR are perfectly collinear, then the beam overlap region is effectively infinite in the propagation direction. In this case, the XUV-IR overlap integral will be positive regardless of any displacement of the sample plane from the focal plane, and maximal when the sample is at the focal plane. However, if there is a small angle $\delta\theta$ between their k -vectors, then the beams will only spatially overlap within a finite region. In this case, the position of the sample plane relative to the beam crossing plane becomes a critical experimental parameter. For an infinitely thick sample (i.e., a chamber effusively filled with gas), it wouldn't matter where the beams crossed as long as they overlapped somewhere within the chamber. Then, the overlap integral would decrease as a function of $\delta\theta$, but it would never go to zero. For a thin sample, the bounds of Eq. (1.18) must enclose the beam overlap region, or else the integral will be zero. Thus, the signal strength of a condensed phase ATAS experiment is roughly 3 orders of magnitude more sensitive to the z -position of the sample relative to the focal plane than a gas phase ATAS experiment.

1.9 Experimental Methods

In this section the methods to find spatial and temporal overlap of the XUV and IR are discussed. Also detailed are the experimental methods for adjusting the pump intensity for a condensed matter sample.

1.9.1 Finding XUV-IR spatial overlap

XUV is ionizing radiation and cannot propagate in air. However, due to macroscopic phase matching conditions, the XUV propagates in the same direction as the IR light that created it. Therefore the initial alignment of the two arms of the interferometer is done by removing the metallic filter in the generation arm and overlapping the two IR foci in the target chamber. This alignment is done as follows.

First, we verify that the laser is pointing correctly into the interferometer using our fiducials.⁴ We remove the sample holder from the target chamber and the metallic filter from the generation arm. This allows the generation arm's IR light to propagate downstream to

⁴Details of this process will be explained in the full dissertation.

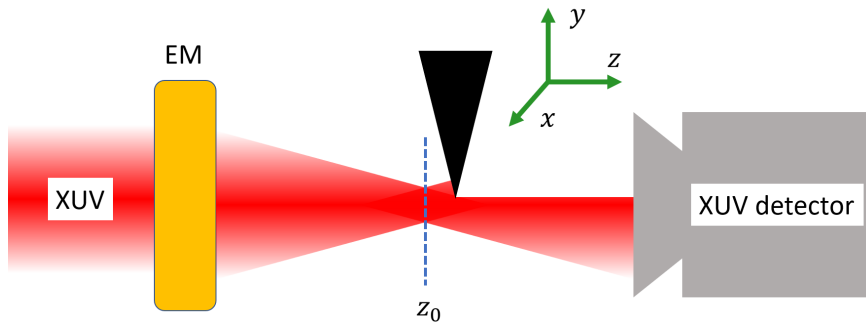


Figure 1.15: Schematic of XUV knife edge measurement. EM: ellipsoidal mirror, z_0 : XUV focal plane.

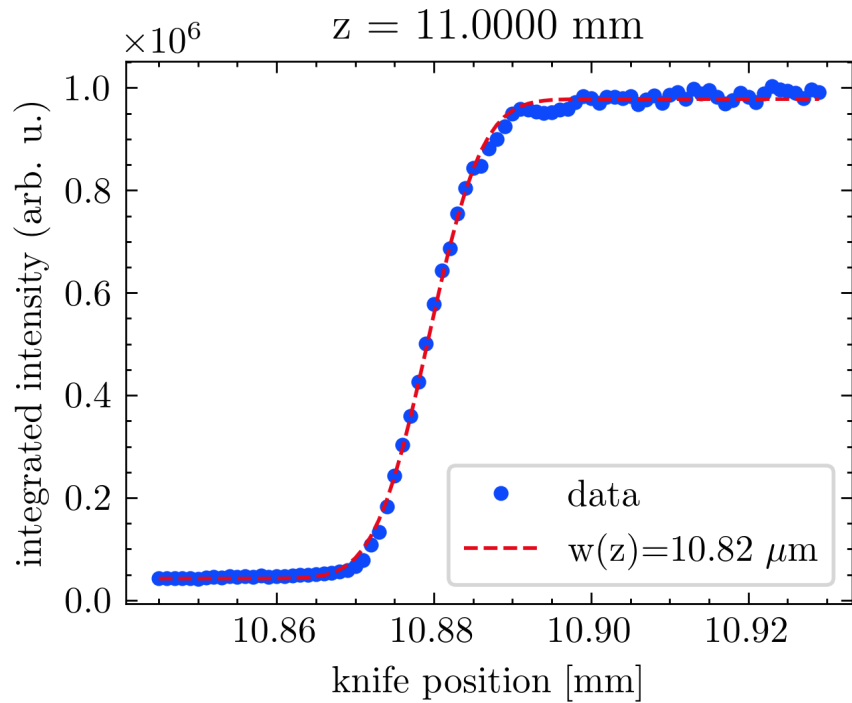


Figure 1.16: A typical XUV knife edge measurement near the focal plane. The sample motor position is $k = 11.0000 \text{ mm}$. A fit to equation Eq. (1.23) yields a beam waist of $10.82 \mu\text{m}$ at this position.

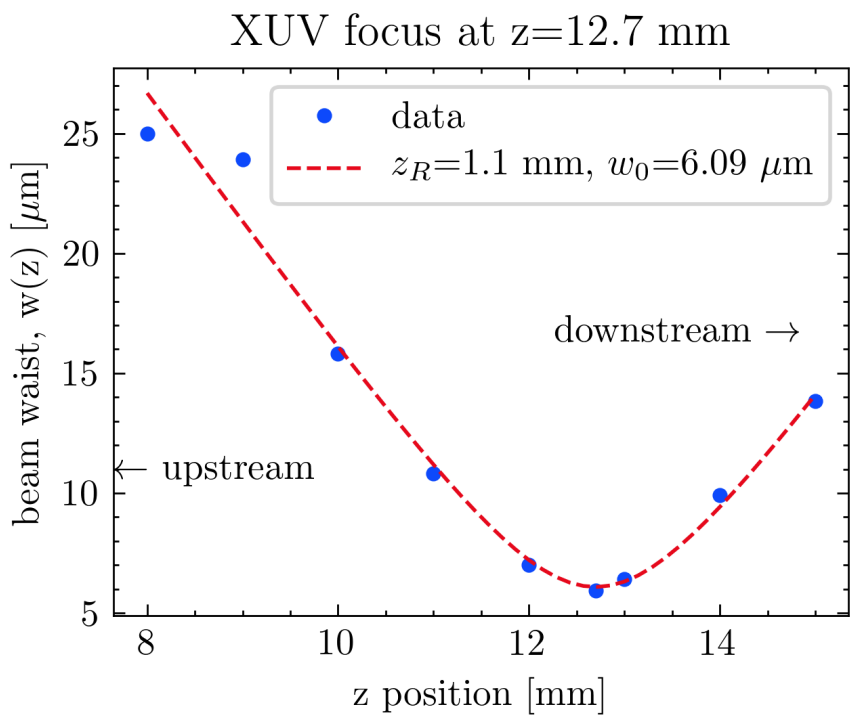


Figure 1.17: Evolution of XUV beam waist as a function of propagation direction, z . The Rayleigh range z_R and beam waist w_0 are extracted from the fit to Eq. (1.22). **question: what is M^2 value of the XUV?**

the target chamber. We then place a pair of reflective and absorptive neutral density filters (OD = 7), a 1 μm low-pass filter (Thorlabs FELH1000) and a digital camera (ImagingSource DMK 27AUJ003) in the target chamber so the sensor is at the focus of the generation arm’s IR light. These temporary optics are common to both arms, so they do not change the relative position of the foci. We close an iris before L3 to limit the intensity and note the position of the centroid of the focus on the camera’s sensor. The generation shutter is closed and this process is repeated for the pump arm, with the power being controlled by the $\lambda/2$ waveplate-polarizer optics. The optical mount for the hole mirror has two vacuum compatible motors (Thorlabs Picomotors), which allow us to remotely change the two angles of this optic. By actuating these motors, we can control the lateral position of the pump arm’s focus relative to the ellipsoidal mirror’s focus. This process is iteratively repeated until the two foci are at the same location on the camera’s sensor.

Due to phase matching, the optimal position of the high harmonic gas source is slightly downstream of the IR’s focal position. As a result, the XUV will focus slightly upstream compared to the generation arm’s IR that we used in the aforementioned alignment procedure. The exact distance between the gas cell and the IR focus depends on many factors, but it is on the few-millimeter scale. The ellipsoidal mirror has a 3:1 demagnification ratio, so for every 1 mm on-axis deviation in the generation chamber, we will have a $1/3^2 = 1/9$ mm on-axis deviation in the target chamber. A correction of this size is within the limit of our target chamber sample motors, but it must be done in vacuum using XUV light.

To this end, we must generate the XUV light that will be used for the upcoming experiment. With the chambers still vented, we verify temporal overlap (described below), and reinstall the sample holder is reinstalled. Finally, the chambers are pumped down and the generation conditions are adjusted to optimize the harmonic flux.

We characterize the XUV focus in the target chamber by performing knife edge measurements at different k -positions, as depicted in Fig. 1.15. We use the interior angled edge of the Si frame on a broken sample heterostructure as a knife edge (see Fig. 1.10). This frame makes an excellent knife edge as it has a very well-defined geometry and fits in the

sample holder. Recalling Gaussian optics, the assumed profile of the XUV beam is:

$$I(x, y, z) = I_0 \left(\frac{w_0}{w(z)} \right)^2 \exp \left(-2((x - x_0)^2 + (y - y_0)^2)/w(z)^2 \right), \quad (1.21)$$

using the coordinate system defined in Fig. 1.15. The XUV focus is at position (x_0, y_0, z_0) .

The beam waist $w(z)$ will evolve as:

$$w(z) = w_0 \sqrt{1 + \left(\frac{z - z_0}{z_R} \right)^2}, \quad (1.22)$$

where z_R is the Rayleigh range. If we use the knife edge to block the transmission as depicted in Fig. 1.15, then the transmitted power will be:

$$P(x, z) = P_0 + \frac{P_{max}}{2} \left(1 - \text{erf} \left(\frac{\sqrt{2}(x - x_0)}{w(z)} \right) \right), \quad (1.23)$$

where x is the insertion of the knife in the beam, z represents the location of the knife plane in the propagation direction, and erf is the error function.

A typical knife edge measurement is shown Fig. 1.16. In this measurement, the knife edge is translated across the XUV spot in 1 μm steps until the XUV light is completely blocked. A 2D spectrum is saved at each knife edge position. Each image is background subtracted, normalized and summed (integrating over all divergences and wavelengths), which yields the XUV flux as a function of knife position. The resulting curve is fit to Eq. (1.23) and the beam waist $w(z)$ is extracted for this z -position.

The knife edge measurement is repeated at different z -positions until enough data has been acquired to determine the focal plane. The evolution of the XUV beam waist is shown in Fig. 1.17. In this figure, the beam waist has been fit to Eq. (1.22) to determine the focal plane z_0 , the Rayleigh range z_R and the beam waist w_0 . In both figures, a reasonably good fit is obtained, indicating that the XUV light has a Gaussian spatial profile near the focus.

It must be verified that the pump arm's IR light focuses to the same focal plane as the XUV. Therefore, the chambers are vented a second time, the sample holder removed, and the digital camera optics and filters installed. The k-position of pump arm's focus is moved up/downstream by moving L4, which is mounted on a translation stage.⁵

⁵The focusing optics in the pump arm are slightly chromatic, so L4 must be adjusted if the wavelength

1.9.2 Finding XUV-IR Temporal Overlap

Temporal overlap can be found under vacuum or in air. In either case, spatial alignment must already be achieved. If the chambers are vented, temporal overlap can be checked using a camera at the focus to observe interference fringes. Note that the presence of air in the generation arm introduces an additional path length of $\approx (3 \text{ m}) \times (n - 1) \approx 820 \mu\text{m}$. Therefore, the pump arm needs to be shortened by moving the retro reflector approximately $(3 \text{ m}) \times (n - 1)/(2n) \approx 410 \mu\text{m}$ to recover overlap when the system is under vacuum.

Overlap can be found under vacuum by routing the IR beam outside of the chamber. A translatable silver mirror, controlled by a set of gears and a linear shift vacuum feedthrough, is used to direct the light through a viewport on the spectrometer chamber wall. The light is focused by a $f = +750 \text{ mm}$ lens (Thorlabs LA1727-C) onto a camera. Note that the spatial profile of the IR beam is not preserved during this routing, as the beam is heavily clipped by a vacuum aperture that separates the target chamber from the spectrometer. As a result, this method *cannot* be used to confirm spatial alignment of the foci. However, enough light makes it through to view interference fringes at overlap.

A BBO crystal, installed in one of the sample holder's sample slots in the target chamber, can also be used to find overlap. The intensity in each arm should be set so that SHG is produced only at temporal and spatial overlap.

1.9.3 Optimization of IR Pump Parameters

The arguments in Section 1.8.2 provide a starting point for the interaction intensity, but the optimum excitation intensity must be determined experimentally by observing how the sample response scales with interaction intensity. Unlike a gas phase sample a condensed phase sample can suffer permanent laser-induced damage, which complicates any intensity investigation. The exact damage mechanism was not studied but we have observed two modes of membrane failure, as shown in Fig. 1.19. Occassionally, the volume near the IR focal spot will be ablated by the laser, leaving the rest of the sample undamaged. The is changed.

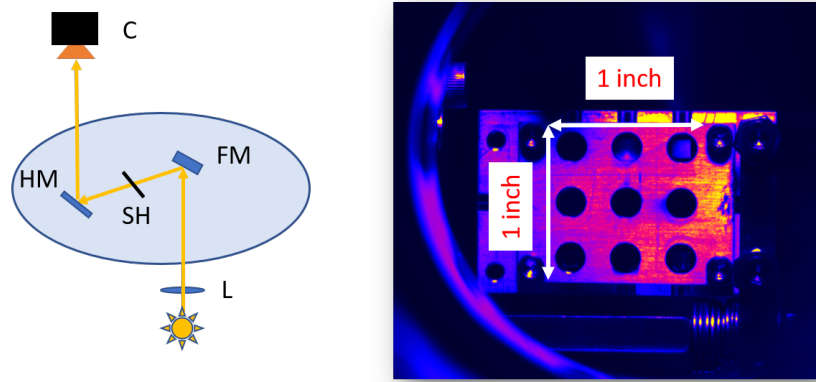


Figure 1.18: *In-situ* imaging of the samples within the target chamber. Left: optical setup for *in-situ* imaging of samples. C: Si CCD camera, HM: hole mirror, SH: sample holder, FM: flip mirror, L: lens. Right: false color image showing the sample holder with a 3 x 3 grid of 5 mm diameter clear apertures. Samples are held in a clamshell design centered in the clear apertures. Samples are backlit using a flashlight.

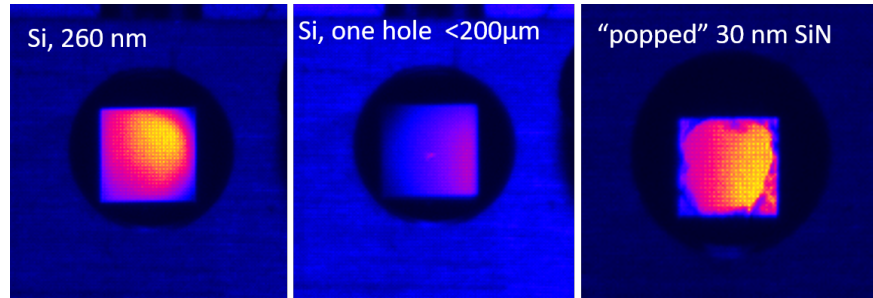


Figure 1.19: False color images showing laser drilled freestanding membranes. Left: pristine 260 nm thick Si membrane (Norcada). Middle: same sample, after performing an IR power scan that exceeded the membrane's damage threshold. A $<200 \mu\text{m}$ hole is visible as a cluster of bright pixels near the center of the membrane. Right: 30 nm SiN membrane after a similar power scan showing a "popped" membrane. The ragged edges near the clear aperture of the frame are all that remain of the membrane. For all images, the apparent brightness gradient across the samples is caused by inconsistent backlighting. Images were taken using the optical setup shown in the left panel of Fig. 1.18.

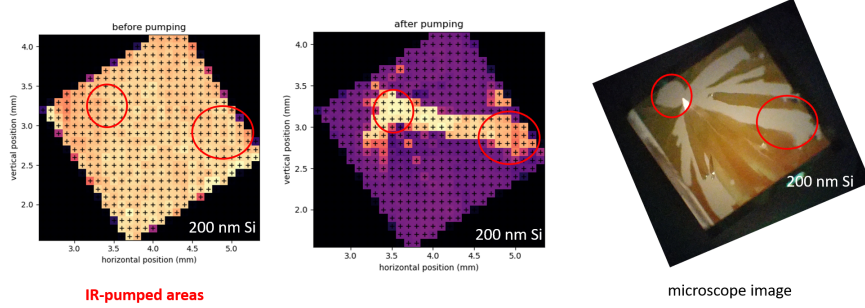


Figure 1.20: Laser damaged 200 nm silicon membrane samples. Left panel: XUV map of pristine Si before being exposed to IR laser. Higher transmission is indicated by brighter colors. Sample is rotated approximately 30 degrees relative to motor axes. Center panel: XUV map of damaged sample after being pumped with $\approx 65 \mu\text{J}$ of $\lambda = 1500 \text{ nm}$ at 1 kHz rep. rate in two locations. Damage occurred within the first camera exposure (2 seconds) and propagated to regions that were not exposed to the laser. Right panel: microscope image of damaged sample (beige) showing large sections of missing material (white). Red circles in all three pictures indicate the two locations that were exposed to IR laser light.

most common failure mode results in the immediate destruction of the entire sample, often within a single camera exposure. Sample damage is apparent in both the visible and the XUV, as shown in Fig. 1.20.

The IR intensity incident on the sample is controlled by a motorized achromatic $\lambda/2$ waveplate (Thorlabs AHWP10M-1600, $\lambda = 1100 - 2000 \text{ nm}$) and a pair of ultra broadband wire grid polarizers (Thorlabs WB25M-UB, each with a 1000:1 extinction ratio for $\lambda = 0.6 - 4 \mu\text{m}$) in the pump arm (see Fig. 1.1). A $1 \mu\text{m}$ longpass filter (Thorlabs FELH1000, OD > 5) is positioned before the waveplate-polarizer assembly to filter out the OPA's visible parasitic wavelengths. During an experiment, the intensity is measured using an InGaAs photodiode (Thorlabs DET10D) mounted with a 2.0 absorptive neutral density filter and $1 \mu\text{m}$ longpass filter (Thorlabs FELH1000), which detects light scattered off a mirror in the pump arm and is monitored using an oscilloscope (LeCroy). Absolute measurements of the average IR power were taken with a power meter (Gentek) located before the diverging lens L4.

As will be described below, the existence of long lived excited states further inhibits the study of ultrafast processes. To this end, ATAS experiments were performed to find the

optimal rep. rate, pulse energy and wavelength.

Feature Scaling with Rep. Rate

We performed exploratory experiments at 1 kHz to determine the optimal excitation pulse energy. Two delay points were recorded: with the XUV and IR pulses overlapped ($\tau = 0$) and with the XUV pulse arriving about 300 fs before the IR ($\tau = -\infty$). For each delay point, we used three pulse energies: 1.03, 1.43 and 1.75 μ J. To increase the signal-to-noise, we performed each experiment 104 times and averaged the datasets. The exposure time was 0.5 seconds, and the sample was rastered so that each measurement was recorded at a new position on the sample. The results are shown Figs. 1.21, 1.22a and 1.22b.

Figs. 1.21a to 1.21d and 1.22a show the average ΔA as a function of the number of averaged measurements, M . Spectral features are apparent after averaging about 10 datasets together, but the fidelity of the signal does not appreciably improve after the first $M = 50$ datasets. Figs. 1.21e and 1.21f show the average signal (lines) and the standard deviation (shaded area), as calculated from the entire ensemble of measurements. The data is noisy, but we can see a spectral feature near 30 eV which scales with pulse energy (or perhaps average power). This behavior is evident in Fig. 1.22b. However, this feature is delay-independent: ΔA has nearly the same value regardless of whether the XUV arrives before or after the IR pulse.

To confirm the delay-independence of this feature, we performed delay scans at two different pulse energies (1.43 and 1.75 μ J). These measurements are shown in Fig. 1.22. Delay was controlled by inserting a fused silica wedge into the interferometer (W in Fig. 1.1). Each delay step corresponds to approximately 3.25 fs (25 μ m of wedge insertion).

The raw data is shown in Figs. 1.22c and 1.22d. As this experiment was only performed once ($M = 1$), the contrast is poor and the 30 eV feature is barely visible. The spectral feature becomes more prominent after performing a rolling average over 20 delay points (65 fs), which is shown in Figs. 1.22e and 1.22f. These delay measurements confirm our suspicion that the absorption feature is delay-independent at 1 kHz.

One possible origin of a delay-independent signal can be a very long-lived excited state.

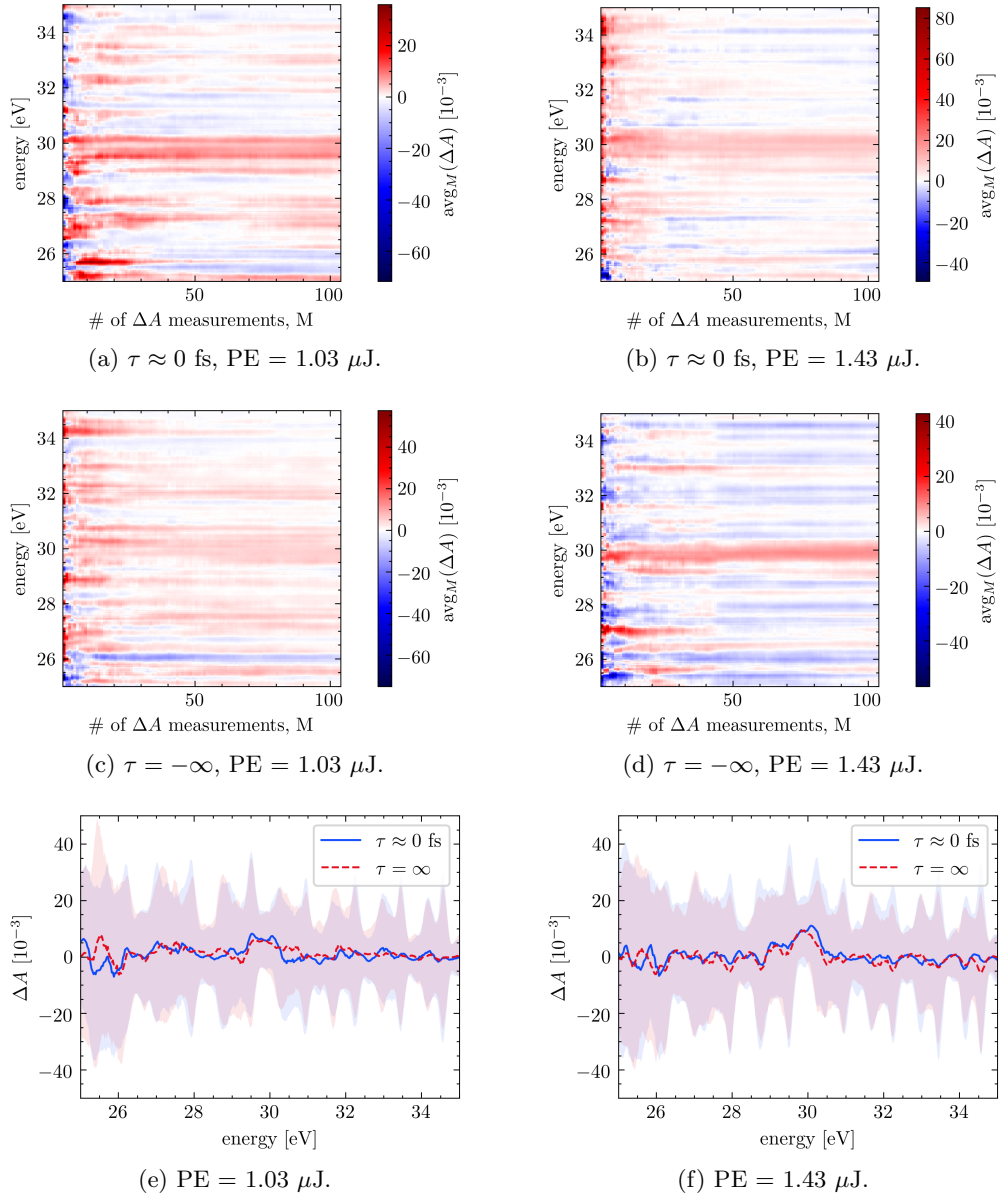


Figure 1.21: 1 kHz fixed-delay ATAS measurements on 100 nm Ge using a $\lambda = 1450$ nm excitation pulse. See text for details.

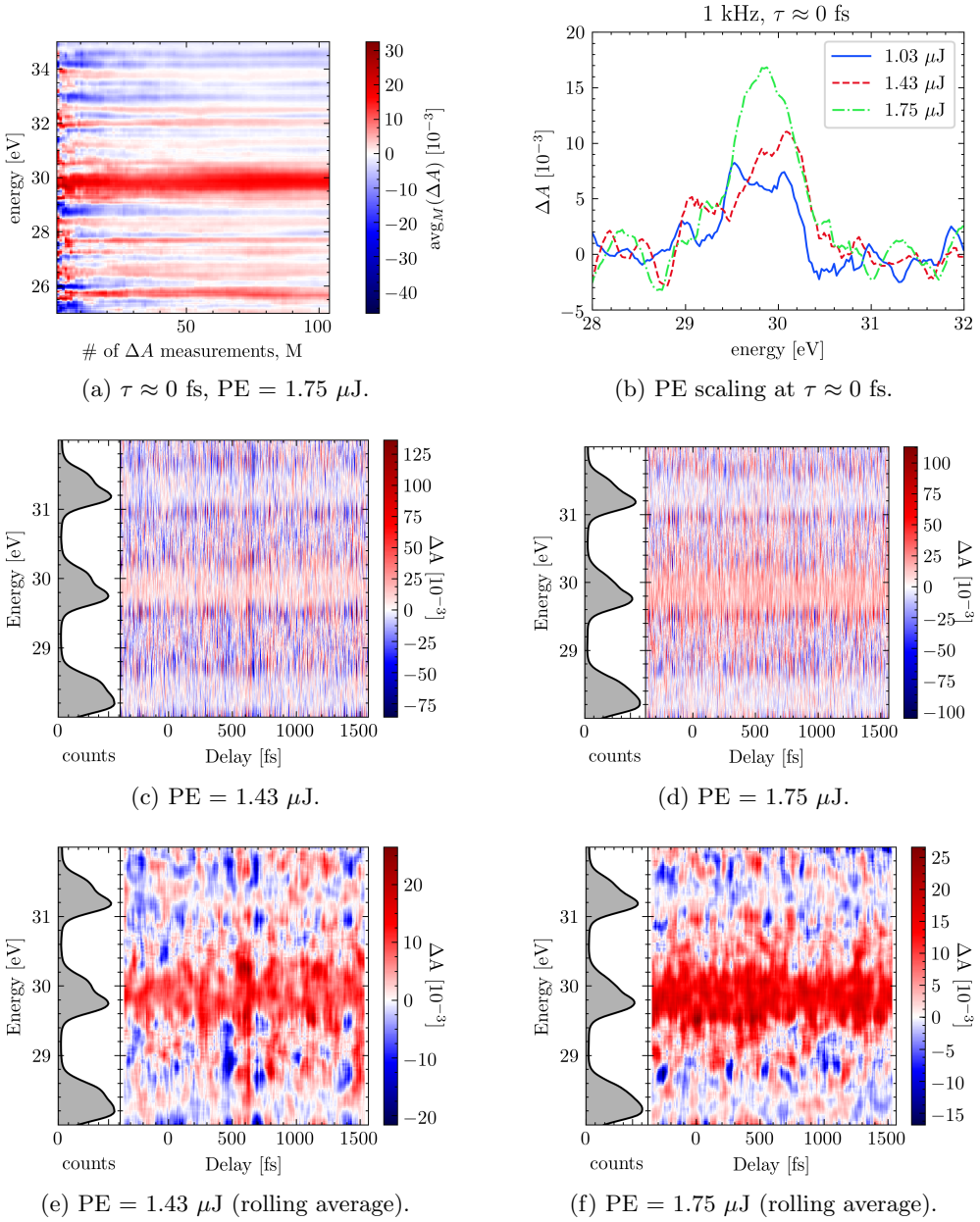


Figure 1.22: 1 kHz ATAS measurements in Ge using a $\lambda = 1450$ nm excitation pulse. Fig. 1.22a: fixed-delay ATAS measurements with a pulse energy of 1.75 μJ . Fig. 1.22b: Pulse energy scaling at overlap of 1 kHz measurements. Figs. 1.22c to 1.22f: delay scans at 1 kHz. Figs. 1.22c and 1.22d: raw delay scan data. Figs. 1.22e and 1.22f: rolling average of the raw data with a 65 fs window (20 delay points). The left panel on each spectrogram shows the XUV spectrum. See text for details.

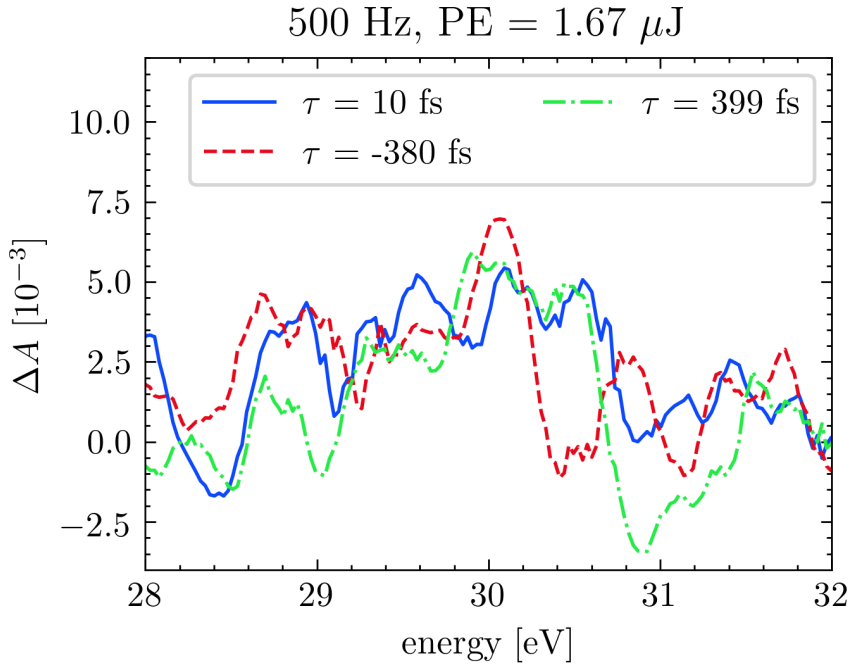


Figure 1.23: 500 kHz ATAS measurements in Ge using a $\lambda = 1450 \text{ nm}$, $1.67 \mu\text{J}$ excitation pulse. Each delay curve is an average of 104 identical measurements. The sample shows no delay dependence within the uncertainty of the measurement.

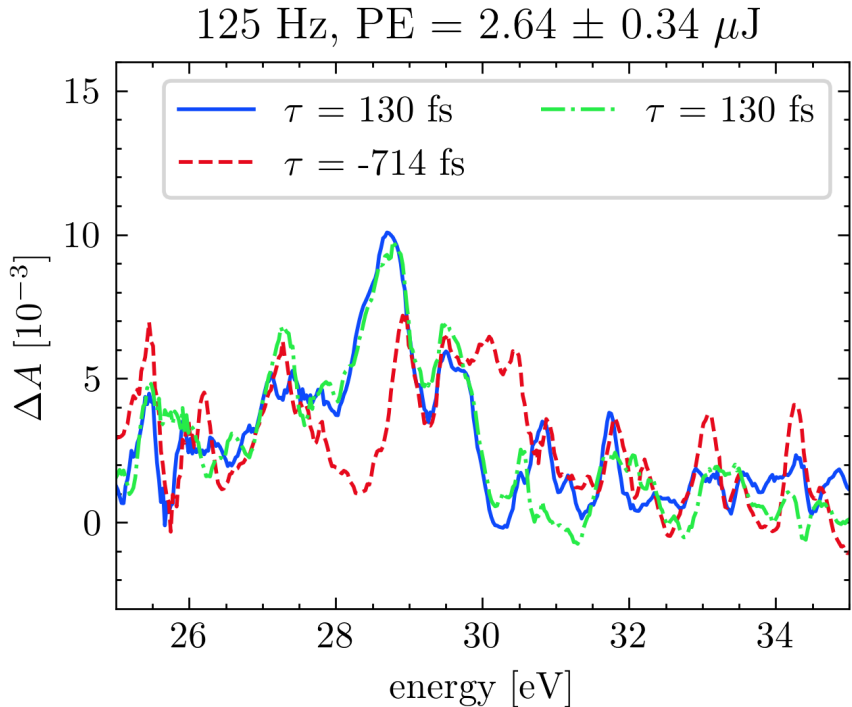


Figure 1.24: 125 Hz ATAS measurements in Ge using a $\lambda = 1450 \text{ nm}$, $2.64 \mu\text{J}$ excitation pulse. Each lineout represents the average of 394 measurements. See text for details.

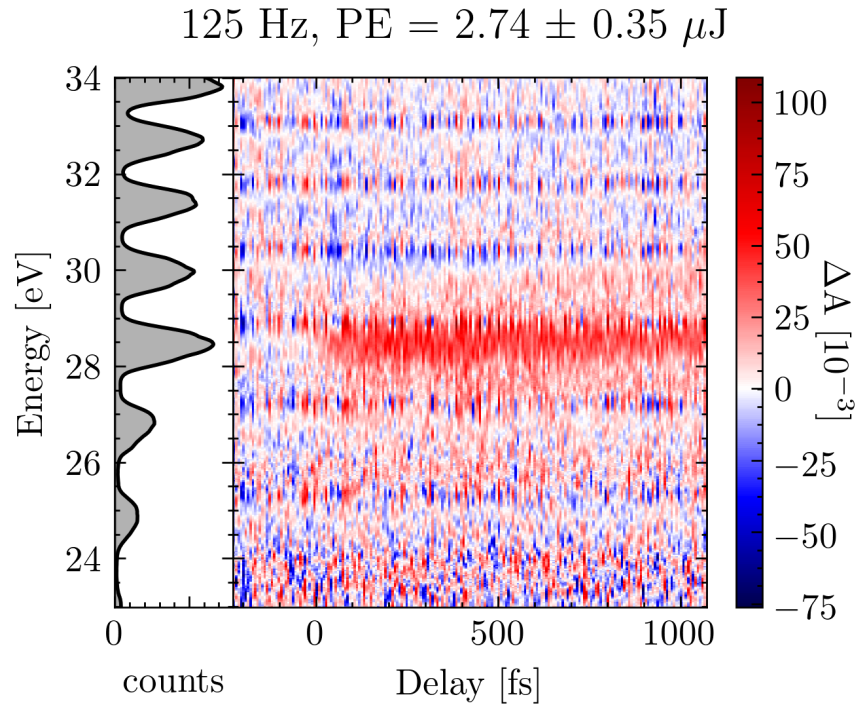


Figure 1.25: 125 Hz delay scan in Ge using a $\lambda = 1450$ nm, $2.74 \pm 0.35 \mu\text{J}$ excitation pulse. This is an average of 3 repeated measurements. See text for details.

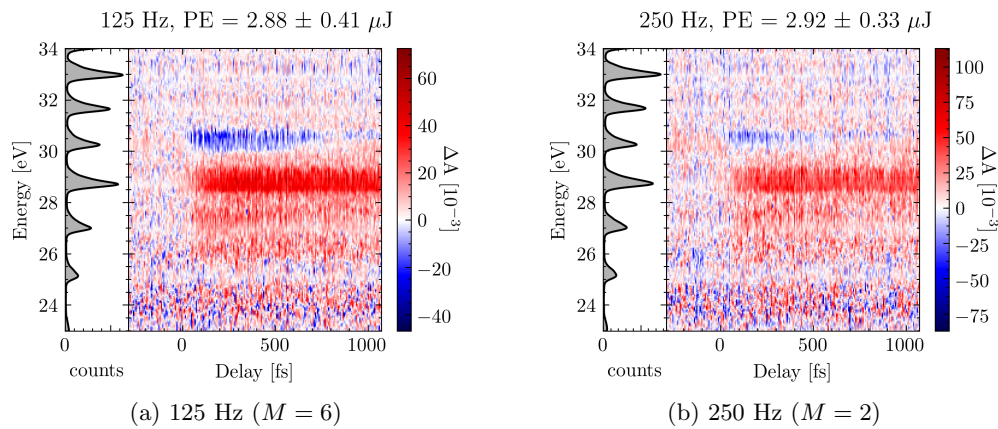


Figure 1.26: 125 vs. 250 Hz measurements at $\lambda = 1430$ nm.

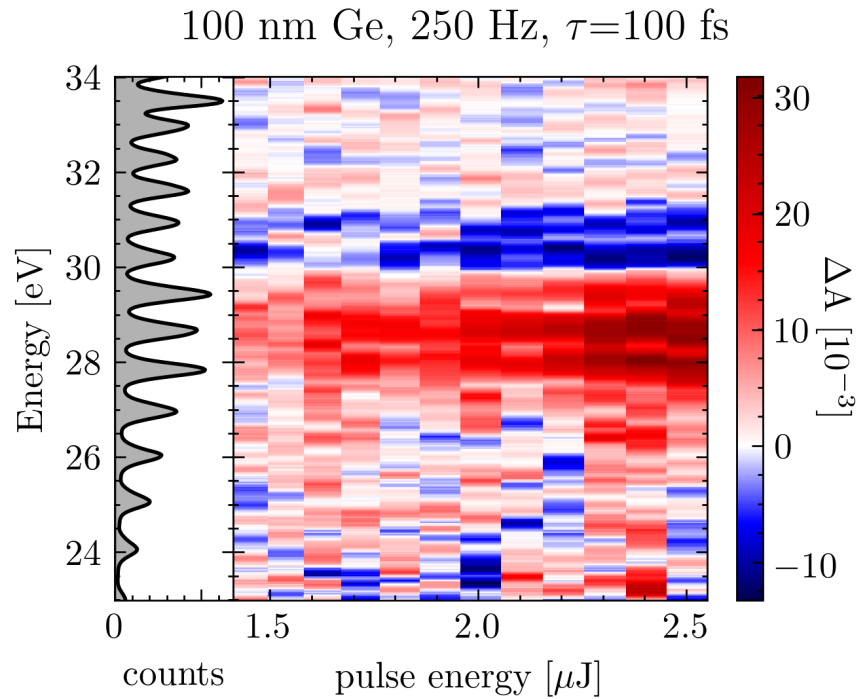


Figure 1.27: Pulse energy scan of 100 nm germanium sample near temporal overlap. Left panel shows the average ground state spectrum, $S_{gs}(E)$. Right panel shows the change in absorbance, $\Delta A(E, PE)$, as a function of pulse energy, PE . Data shown in this figure is the average of 20 identical measurements: individual datasets were background subtracted and normalized for exposure time before being averaged; no additional data processing was performed on this dataset. See text for details.

Each laser shot initiates an assortment of electron and phonon dynamics, each with their own time scales. If any of these excited states have time scales that approach the inverse rep. rate of the laser ($1/RR$), then the dynamics from the previous shot will still be evolving by time the next shot arrives. Since each exposure integrates over hundreds or thousands of laser shots, measurements at a nominal delay τ will contain information from several delays, each separated by the time between laser shots: $\tau, \tau - 1/RR, \tau - 2/RR, \dots$. If this is the case, then the magnitude of the delay-independent signal should decrease as time between laser shots is increased. As the time between laser shots is increased past the lifetime of the state, the excited state population from the previous laser shot will be small enough to observe the dynamics of the shorter-lived states. Experimentally, we can accomplish this by adjusting the rep. rate divider on the Spitfire amplifier (which reduces the rep. rate), and/or using an optical chopper.

The rep. rate was halved to 500 Hz using the Spitfire's rep rate divider ($m = 2$) and the exposure time was doubled to 1 second so that the number of laser shots per exposure was held constant. A series of fixed-delay measurements were recorded using a $1.67 \mu\text{J}$ pulse energy, shown in Fig. 1.23. The spectral feature at 30 eV is still present, but it does not exhibit any delay dependence within the uncertainty of the measurement. It is notable that, for a similar pulse energy, the magnitude of the feature at 500 Hz is half that of the 1 kHz measurement. This is consistent with the hypothesis of a long-lived state contributing to the signal.

The rep. rate was lowered to 125 Hz using a combination of the rep. rate divider ($m = 4$) and an optical chopper ($T = 50\%$) placed after the TOPAS. The exposure time was increased to 4 seconds to maintain sufficient counts on the detector. An ATAS spectrum was recorded about 130 fs after temporal overlap and several hundred fs before overlap using a $2.64 \pm 0.34 \mu\text{J}$ excitation pulse ($\lambda = 1450 \text{ nm}$), as shown in Fig. 1.24. A second measurement after overlap was recorded to ensure repeatability. At negative delays (red curve), we see the familiar 30 eV feature, albeit weaker at 6×10^{-3} . Near overlap, we see a new feature emerge at 28.7 eV, with a magnitude of $\approx 10 \times 10^{-3}$. This observation is consistent with long-lived excited state at 30 eV. A delay scan at 125 Hz, shown in Fig. 1.25, reveals that

this feature is indeed time-dependent with a ps-scale lifetime.

The fundamental wavelength was decreased 20 nm to 1430 nm, where the absorption length in Ge is about 5% shorter. For a fixed pulse energy, this increases the excitation fraction and thus the strength of the ΔA signal. Using this shorter wavelength we can observe a more robust sample response, as shown in Fig. 1.26.

At 1430 nm, we can see a broad spectral response from 25.7 to 31 eV. From 25.7 to 30 eV, there is a broad increase in absorption, with the largest increase occurring between 28.4 and 29.5 eV. A decrease in absorption occurs between 30 and 31 eV. These features are present in both the 125 and 250 Hz data. The 30 eV negative delay feature persists in the 250 Hz dataset, but at 12×10^{-3} it does not overwhelm the rest of the sample response. Further measurements were performed at 250 Hz, which provides a good compromise between and data collection time.

A two-color generation technique was employed to double the spectral content of the XUV. This was done by placing a BBO crystal, 200 μm of calcite and a zero order 1310 nm $\lambda/2$ waveplate between L3 and the generation chamber vacuum window. This generation scheme provided more spectral coverage of the sample response function. Under these conditions, a pulse energy scan was performed, as shown in Fig. 1.27.

Ge-specific experimental parameters: wavelength, generation conditions, exposure time, MCP settings, rep rate, etc.

calculated excitation percentage, from lens calculations and measured IR power.
does the measured signal strength make sense? i.e., order of magnitude
show pictures of popped membranes. show delay spectrograms of drilled out samples.
you can talk about high average power damage and high peak power damage. no plots,
but maybe mention the parameters that led you to believe that you were operating at the
boundary between those two regimes.

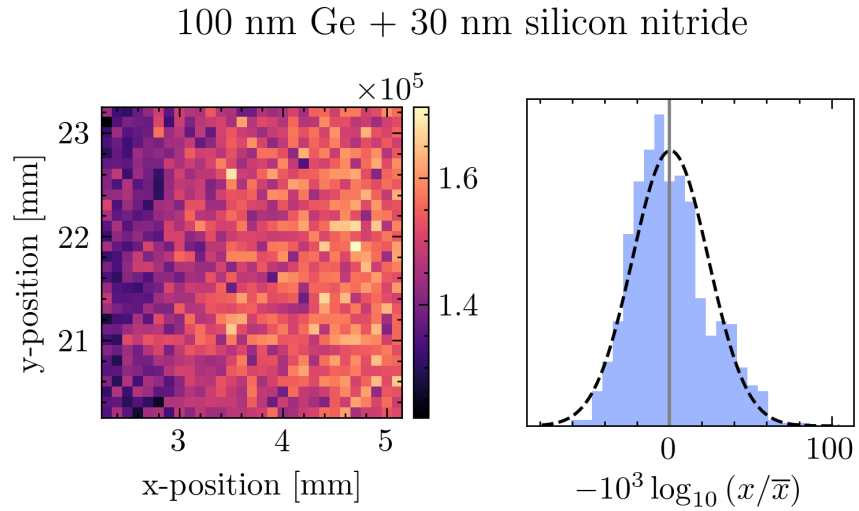


Figure 1.28: Left panel: spatial mapping of integrated XUV counts (**integrated over what energy range?**) of a 100 nm Ge + 30 nm silicon nitride sample. Right panel: histogram of values from the left panel.

data pipeline figure
- shows
PumpOn/Off
images, lineouts,
filtering, etc.

Figure 1.29: this figure shows the data processing pipeline. it shows how we start with PumpOn-Off 2D images and transform them into spectrograms. it includes steps like an absorbance (A) calculation, spectral lineouts, frequency filtering and smooth, energy calibration, etc.

top: pump on & pump off lineouts
bottom: delta-OD calculation.

Figure 1.30: this figure shows, using real data, a pump off and pump on spectral lineout. in another panel, it shows the ΔA .

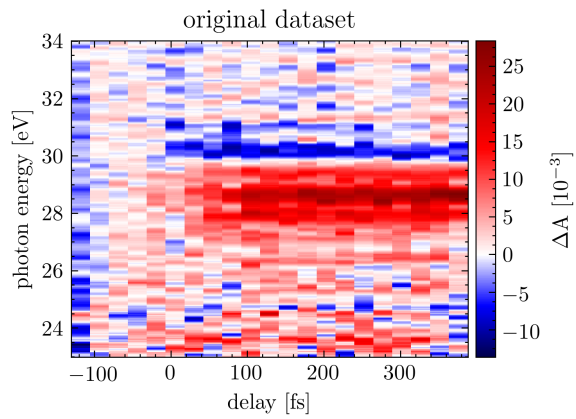


Figure 1.31: $N = 50$ averaged delay scans. no corrections have been made to the data

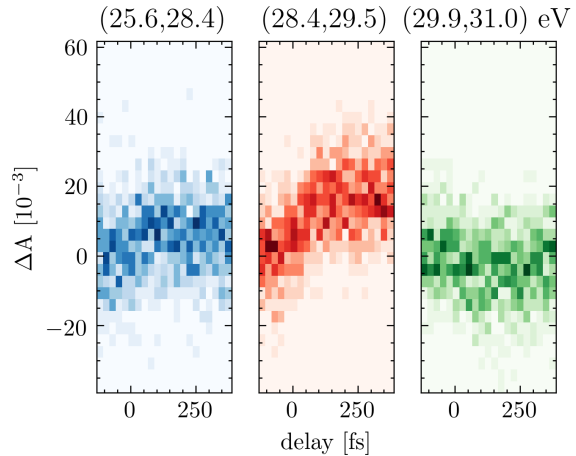


Figure 1.32: $N = 50$ averaged delay scans. no corrections have been made to the data. histogram of ΔA for 3 selected features. dataset is same as Fig. 1.31.

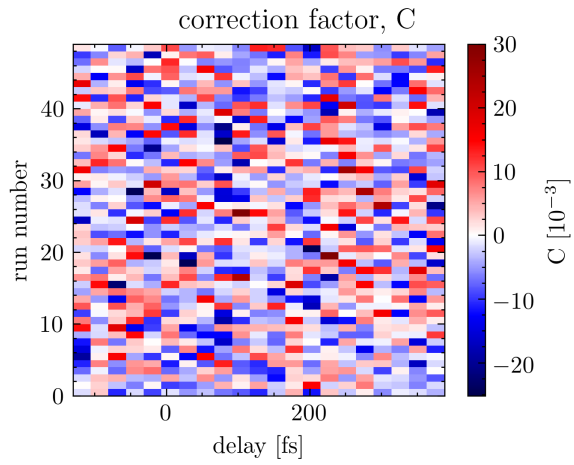


Figure 1.33: correction factor, $C(\tau, E)$, from Eq. (1.28).

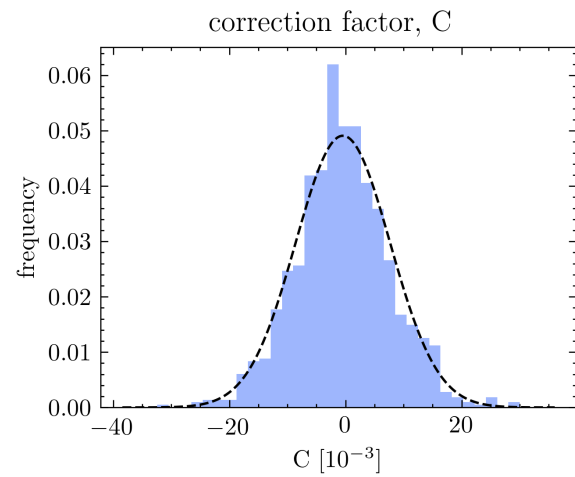


Figure 1.34: histogram of correction factor, $C(\tau, E)$, values from Eq. (1.28).

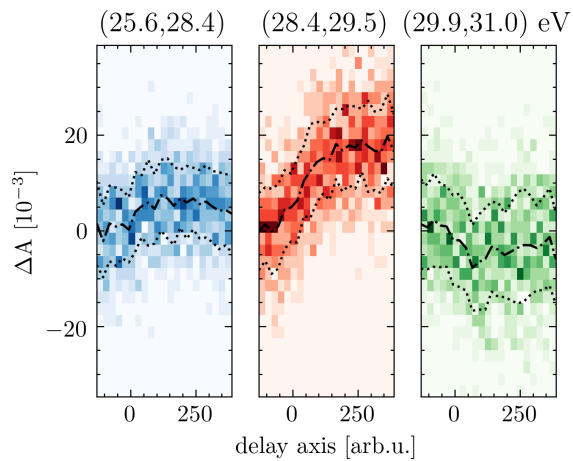


Figure 1.35: histogram of spectral features from dataset with correction factor $C(\tau, E)$ applied

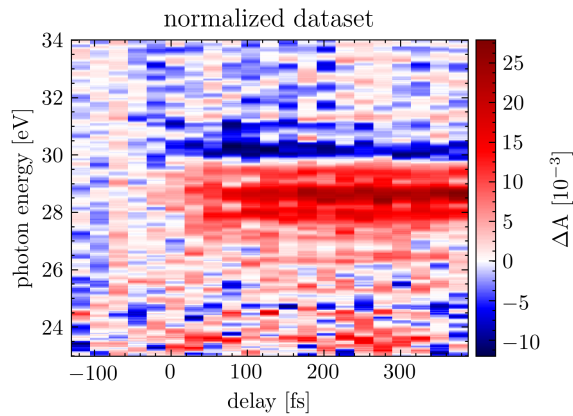


Figure 1.36: normalized dataset: dataset with correction factor $C(\tau, E)$ applied

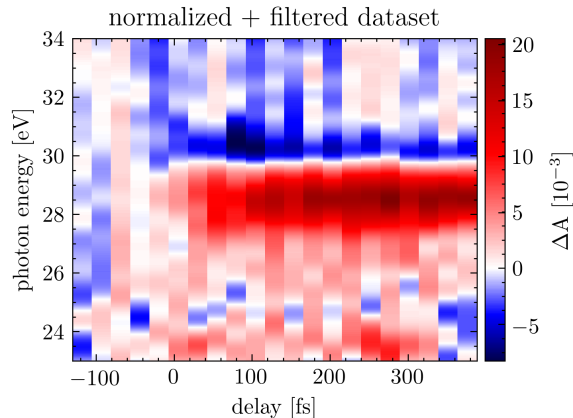


Figure 1.37: normalized dataset with frequency filter applied

1.10 Data Processing

$N = 50$ dataset experimental parameters: $\lambda = 1430$ nm, Spitfire rep. rate = 125 Hz, pump energy (before focusing optics) $\sim 2.9 \mu\text{J}$ per pulse, camera exposure time = 3 seconds. each run took about 6 minutes for a total collection time of about 5 hours.

The XUV photon spectrometer utilizes a flat field grating (Hitachi, 1200 l/mm) to spectrally disperse the XUV light. The grating is designed to focus along the spectral axis (horizontal direction of sensor) while preserving the spatial profile of the beam (vertical direction). The focus of the grating is incident on a 75 mm diameter imaging quality microchannel plate (MCP) array (Photonis), which converts the XUV photons into electrons via a nonlinear avalanche process with a gain of approximately $10^6 - 10^8$. These electrons are accelerated towards a phosphor screen, which converts the electrons into visible photons with a central wavelength of ~ 480 nm. The visible photons exit the vacuum chamber via a glass feedthrough and are imaged by a lens onto a CMOS sensor of a digital camera (Andor). The recorded data is a two dimensional array of counts, with the horizontal axis representing the spectral content and the vertical axis representing the spatial profile of the beam.

talk about all the steps you use to process the data, starting from the 2d image and ending with the delta-A spectrogram.

1. calibration of spectrometer energy axis and delay axis (just state it as fact, don't go into detail)
2. data reduction: 2D image to 1D spectral lineout for each measurement. note that the jacobian needs to be used for plotting counts vs energy, but not for ΔA or A since it divides out
3. investigation of noise: peaks vs valleys vs slopes of harmonics. most of the noise comes from not the peaks, so we use the value at the peak for later analysis
4. sample drilling or harmonic drift? inconclusive? or *no conclusive evidence of drilling?*

5. correlations between different harmonic peaks in ΔA
6. linear correction method $C(\tau, E)$
7. choice of $\text{dx}=2$ method
8. frequency filtering
9. failed methods: SVD, interpolation

1.10.1 energy and delay calibration

1.10.2 A note about the Jacobian

At each pixel, the spectrometer's camera records the integrated counts within the area of one pixel. We wish to convert the measured dataset (counts *vs.* spectral pixel) to a physically meaningful spectrum (counts *vs.* photon energy) while conserving energy [10].

More precisely, our measurement samples a counts function f_p in the spectral pixel basis p :

$$f_p(p) : \text{spectral pixel} \rightarrow \text{counts}. \quad (1.24)$$

The spectral pixel value is proportional to wavelength, with some extra factors that account for the geometry of the detector relative to the grating. We can convert the domain of the spectrometer's dataset from spectral pixels p to energy E (in eV) using an invertible polynomial transformation⁶:

$$\begin{aligned} E(p) &: \text{spectral pixel} \rightarrow \text{energy [eV]}, \\ E(p) &= a_4 p^4 + a_3 p^3 + a_2 p^2 + a_1 p + a_0. \end{aligned} \quad (1.25)$$

Let the inverse of $E(p)$ be $p(E)$. From energy conservation, the transformation must preserve the integrated counts:

$$f_p(p) dp = f_E(E) dE. \quad (1.26)$$

⁶The details surrounding the choice of this transformation will be discussed elsewhere in the dissertation.

Rearranging, we obtain an expression for the counts expressed in the energy domain, f_E :

$$f_E(E) = f_p(p) \frac{dp}{dE} = f_p(p) \frac{d}{dE} p(E). \quad (1.27)$$

Therefore, the measured spectrum $f_p(p)$ in the pixel basis can be converted to the energy basis by multiplying it by a factor of $\frac{d}{dE} p(E)$. Note that this factor is only important when considering spectrometer counts; calculations of A or ΔA can omit the Jacobian as it is common to both spectra and will divide out.

1.10.3 source of noise

1.10.4 sample drilling or random drift?

1.10.5 correlations between harmonic peaks in ΔA

1.10.6 integration vs summation near harmonic peaks

1.10.7 apparent ω and 2ω oscillations in data

mention calibration of spectrometer in passing, 2D image \rightarrow 1D spectrum. jacobian needs to be used for plotting counts vs energy, but not for delta-OD, OD or transmission figures.

$$\Delta A^{\text{meas}}(\tau, E) = -\log_{10} \left(\frac{I_{on}}{I_{off}} \right) = \Delta A^{\text{norm}}(\tau, E) + C(\tau, E) \quad (1.28)$$

BIBLIOGRAPHY

- [1] NSM Archive - Physical Properties of Semiconductors.
<http://www.ioffe.ru/SVA/NSM/Semicond/index.html>.
- [2] D. R. Austin, K. R. P. Kafka, Y. H. Lai, Z. Wang, C. I. Blaga, and E. A. Chowdhury. Femtosecond laser damage of germanium from near- to mid-infrared wavelengths. *Opt. Lett., OL*, 43(15):3702–3705, Aug. 2018.
- [3] Y.-H. Chiu, N. G. Minutillo, R. E. Williams, G. J. Smith, D. W. McComb, J. A. Carlin, E. Johnston-Halperin, and F. Yang. Photoluminescence evolution in GaAs/AlGaAs core/shell nanowires grown by MOCVD: Effects of core growth temperature and substrate orientation. *Journal of Crystal Growth*, 429:1–5, Nov. 2015.
- [4] S. K. Cushing, A. Lee, I. J. Porter, L. M. Carneiro, H.-T. Chang, M. Zürch, and S. R. Leone. Differentiating Photoexcited Carrier and Phonon Dynamics in the Δ , L , and Γ Valleys of Si(100) with Transient Extreme Ultraviolet Spectroscopy. *J. Phys. Chem. C*, 123(6):3343–3352, Feb. 2019.
- [5] E. G. Gamaly, A. V. Rode, B. Luther-Davies, and V. T. Tikhonchuk. Ablation of solids by femtosecond lasers: Ablation mechanism and ablation thresholds for metals and dielectrics. *Physics of Plasmas*, 9(3):949–957, Feb. 2002.
- [6] E. Gullikson. CXRO X-Ray Interactions With Matter.
http://henke.lbl.gov/optical_constants/.
- [7] M. Harb, R. Ernstorfer, T. Dartigalongue, C. T. Hebeisen, R. E. Jordan, and R. J. D.

- Miller. Carrier Relaxation and Lattice Heating Dynamics in Silicon Revealed by Femtosecond Electron Diffraction. *J. Phys. Chem. B*, 110(50):25308–25313, Dec. 2006.
- [8] C. J. Kaplan, P. M. Kraus, A. D. Ross, M. Zürch, S. K. Cushing, M. F. Jager, H.-T. Chang, E. M. Gullikson, D. M. Neumark, and S. R. Leone. Femtosecond tracking of carrier relaxation in germanium with extreme ultraviolet transient reflectivity. *Phys. Rev. B*, 97(20):205202, May 2018.
- [9] L. Keldysh. Ionization in the Field of a Strong Electromagnetic Wave. *SOVIET PHYSICS JETP*, 20:1307–1314, May 1965.
- [10] J. Mooney and P. Kambhampati. Get the Basics Right: Jacobian Conversion of Wavelength and Energy Scales for Quantitative Analysis of Emission Spectra. *J. Phys. Chem. Lett.*, 4(19):3316–3318, Oct. 2013.
- [11] E. Nichelatti. Complex refractive index of a slab from reflectance and transmittance: Analytical solution. *J. Opt. A: Pure Appl. Opt.*, 4(4):400–403, July 2002.
- [12] T. N. Nunley, N. S. Fernando, N. Samarasinha, J. M. Moya, C. M. Nelson, A. A. Medina, and S. Zollner. Optical constants of germanium and thermally grown germanium dioxide from 0.5 to 6.6eV via a multisample ellipsometry investigation. *Journal of Vacuum Science & Technology B, Nanotechnology and Microelectronics: Materials, Processing, Measurement, and Phenomena*, 34(6):061205, Nov. 2016.
- [13] M. Schultze, K. Ramasesha, C. D. Pemmaraju, S. A. Sato, D. Whitmore, A. Gandman, J. S. Prell, L. J. Borja, D. Prendergast, K. Yabana, D. M. Neumark, and S. R. Leone. Attosecond band-gap dynamics in silicon. *Science*, 346(6215):1348–1352, Dec. 2014.
- [14] G. Vdovin, F. van Goor, and Guyskk. LightPipes for Python. Flexible Optical.
- [15] M. Volkov, S. A. Sato, F. Schlaepfer, L. Kasmi, N. Hartmann, M. Lucchini, L. Gallmann, A. Rubio, and U. Keller. Attosecond screening dynamics mediated by electron localization in transition metals. *Nat. Phys.*, pages 1–5, Aug. 2019.

- [16] M. Zürch, H.-T. Chang, L. J. Borja, P. M. Kraus, S. K. Cushing, A. Gandman, C. J. Kaplan, M. H. Oh, J. S. Prell, D. Prendergast, C. D. Pemmaraju, D. M. Neumark, and S. R. Leone. Direct and simultaneous observation of ultrafast electron and hole dynamics in germanium. *Nat Commun*, 8(1):15734, Aug. 2017.
- [17] M. Zürch, H.-T. Chang, P. M. Kraus, S. K. Cushing, L. J. Borja, A. Gandman, C. J. Kaplan, M. H. Oh, J. S. Prell, D. Prendergast, C. D. Pemmaraju, D. M. Neumark, and S. R. Leone. Ultrafast carrier thermalization and trapping in silicon-germanium alloy probed by extreme ultraviolet transient absorption spectroscopy. *Structural Dynamics*, 4(4):044029, July 2017.